

AD-A059 969

ARMY ELECTRONICS RESEARCH AND DEVELOPMENT COMMAND WS--ETC F/G 4/1
WATER VAPOR ABSORPTION COEFFICIENTS AT HF LASER WAVELENGTHS. PA--ETC(U).
MAY 78 W R WATKINS, R L SPELLICY, K O WHITE
ERADCOM/ASL-TR-0007-PT-1

UNCLASSIFIED

NL

1 OF 2
ADA
059969



AD A059969

ERADCOM/

ASL-TR-0007-PT-1

AD

Reports Control Symbol
OSD-1366

**WATER VAPOR ABSORPTION
COEFFICIENTS AT HF LASER WAVELENGTHS
PART I: ATMOSPHERIC CONDITIONS
CORRESPONDING TO ALTITUDES UP TO 7 km**

LEVEL

MAY 78

DDC FILE COPY

11 16 11 16 11 02 B 53A

By

Wendell R. Watkins,
Robert L. Spellicy*,
Kenneth O. White,
Brian Z. Sojka
Lanny R. Bower

DDC
OCT 12 1978
RESERVED
F

*Science Applications, Inc.

Ann Arbor, MI, and White Sands Missile Range, NM

Approved for public release; distribution unlimited.



US Army Electronics Research and Development Command
Atmospheric Sciences Laboratory

White Sands Missile Range, N.M. 88002

10 4

045

110663

NOTICES

Disclaimers

The findings in this report are not to be construed as an official Department of the Army position, unless so designated by other authorized documents.

The citation of trade names and names of manufacturers in this report is not to be construed as official Government indorsement or approval of commercial products or services referenced herein.

Disposition

Destroy this report when it is no longer needed. Do not return it to the originator.

SECURITY CLASSIFICATION OF THIS PAGE (When Data Entered)

REPORT DOCUMENTATION PAGE		READ INSTRUCTIONS BEFORE COMPLETING FORM
1. REPORT NUMBER ASL-TR-0007	2. GOVT ACCESSION NO.	3. RECIPIENT'S CATALOG NUMBER
4. TITLE (and Subtitle) WATER VAPOR ABSORPTION COEFFICIENTS AT HF LASER WAVELENGTHS. PART I: ATMOSPHERIC CONDITIONS CORRESPONDING TO ALTITUDES UP TO 7 km		5. TYPE OF REPORT & PERIOD COVERED R&D Technical Report
7. AUTHOR(s) Wendell R. Watkins, Robert L. Spellicy*, Kenneth O. White, Brian Z. Sojka, Lanny R. Bower		6. PERFORMING ORG. REPORT NUMBER
9. PERFORMING ORGANIZATION NAME AND ADDRESS Atmospheric Sciences Laboratory, White Sands Missile Range, NM 88002; *Science Applications, Inc., Ann Arbor, MI, and White Sands Missile Range, NM		8. CONTRACT OR GRANT NUMBER(s)
11. CONTROLLING OFFICE NAME AND ADDRESS US Army Electronics Research and Development Command Adelphi, MD 20783		10. PROGRAM ELEMENT, PROJECT, TASK AREA & WORK UNIT NUMBERS DA Task No. 1L161102B53A
14. MONITORING AGENCY NAME & ADDRESS (if different from Controlling Office)		12. REPORT DATE May 1978
		13. NUMBER OF PAGES 95
		15. SECURITY CLASS. (of this report) UNCLASSIFIED
		15a. DECLASSIFICATION/DOWNGRADING SCHEDULE
16. DISTRIBUTION STATEMENT (of this Report) Approved for public release; distribution unlimited.		
17. DISTRIBUTION STATEMENT (of the abstract entered in Block 20, if different from Report)		
18. SUPPLEMENTARY NOTES		
19. KEY WORDS (Continue on reverse side if necessary and identify by block number) Absorption HF laser Water vapor Atmospheric optics Laser Infrared sub 3-2 sub 1-0		
20. ABSTRACT (Continue on reverse side if necessary and identify by block number) Water vapor absorption measurements are reported at nine HF laser wavelengths ranging from P ₃₋₂ (5) at 3418.1600/cm ⁻¹ to P ₁₋₀ (4) at 3788.2253/cm ⁻¹ . The results were obtained with a temperature controlled longpath absorption cell and a path differencing technique with path differences ranging from 8 to 152 m. Cell temperatures ranging from -18°C to 25°C were used. Pure water vapor as well as air (N ₂ /O ₂) broadened water vapor absorptions were measured for pres- sures ranging from less than 1 torr to 764 torr. Limited data on O ₂ broadened		

DD FORM 1 JAN 73 1473 EDITION OF 1 NOV 65 IS OBSOLETE

SECURITY CLASSIFICATION OF THIS PAGE (When Data Entered)

ABSTRACT (cont)

water vapor absorption as well as pure and air broadened CO_2 absorption are presented. In general the air broadened water vapor results show more absorption than predicted and imply a "super" Lorentz or Voigt line shape. The pure O_2 broadened water vapor absorption is less than the air broadened absorption. New self- and foreign-broadening coefficients are obtained. Finally, the limited CO_2 absorption observed shows good agreement with theoretical predictions. These results will allow more accurate modelling of atmospheric transmission for EO and HEL applications.

ACCESSION for	
NTIS	White Section <input checked="" type="checkbox"/>
DDC	Buff Section <input type="checkbox"/>
UNANNOUNCED	<input type="checkbox"/>
JUSTIFICATION	
BY	
DISTRIBUTION/AVAILABILITY CODES	
CONFIDENTIAL	SECRET
A	

ERRATA SHEET FOR ASL-TR-0007

WATER VAPOR ABSORPTION COEFFICIENTS
AT THE HF LASER WAVELENGTHS PART 1:
ATMOSPHERIC CONDITIONS CORRESPONDING
TO ALTITUDES UP TO 7 KM

Page 5, 10th line on page

Third word from end of line is "laser."

Fifteenth line on page, second and third words in line are "diameter"
and "hole."

Page 7, next to last line on page

Change "After reflecting off" to "After reflecting from."

Page 11, figure 5

Add "a" underneath drawing on left and "b" underneath drawing on right.

Page 20, 9th line from top of page, end of line

Change "32 m" to "24 m."

10th line, beginning of line, change "7-spot" to "5-spot."

Page 28, 2nd line from top

Change "contributions" to "contribution."

Page 29, equation (8)

Change Π to Π .

Page 30, 7th line from top

Delete "and" from end of line.

Page 34, table 3, last column, fourth entry

Change 6.30 to 7.12.

Pages 37 and 38

Replace figures 16, 17, 18, and 19 with new figures furnished.

78 10 4 045

Page 41, equation (16)

Change c to C and Π to π .

Page 45, 5th and 6th lines from top

Change to read "... the calculated coefficients at laser line $P_1(7)$ were"

Page 58, 3rd and 4th lines from top

Change to read "... as the water vapor concentration (and hence temperature) varies, decreasing rapidly"

Page 61, 14th line from top, first word in line

Change "to" to "into."

Page 76, figure B-7, 2nd line of figure caption

"line $P_2(8)$ "

Page 77, footnote underneath table

Add the following statement: "Table entries include line fit values for those cases in which the data were more than 10% different from the fit values."

Page 83, reference 4, last line

Change 1956 to 1596.

Page 84, reference 18, first line

Change "Monchromatic" to Monochromatic."

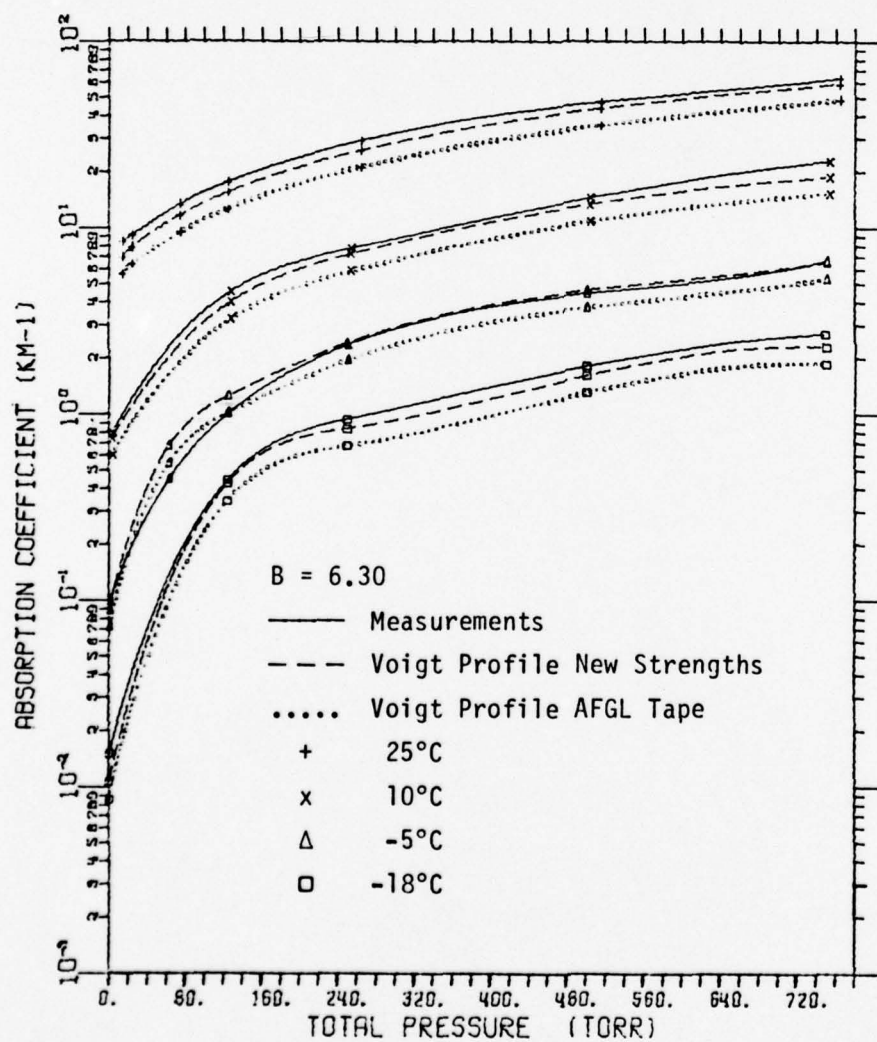


Figure 16. Measured absorption coefficients and calculated Voigt predictions for HF laser line $P_2(5)$ using standard and modified AFGL line tabulations.

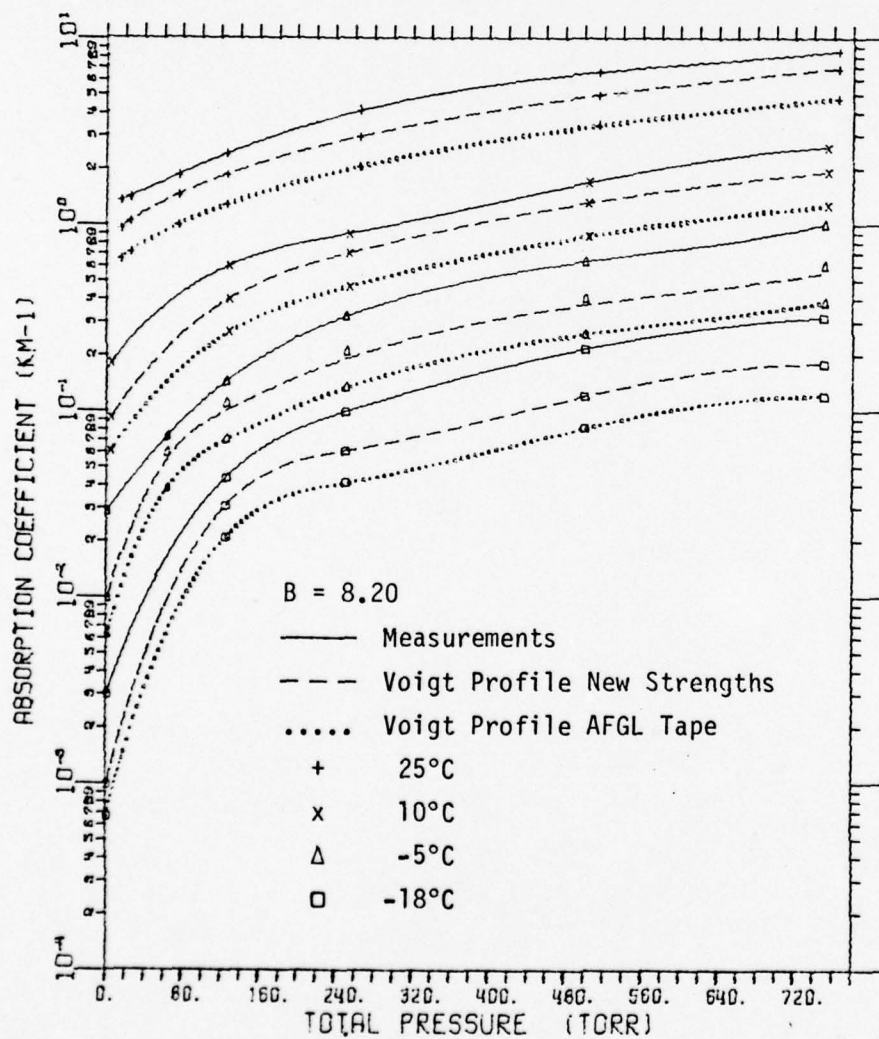


Figure 17. Measured absorption coefficients and calculated Voigt predictions for HF laser line $P_2(7)$ using standard and modified AFGL line tabulations.

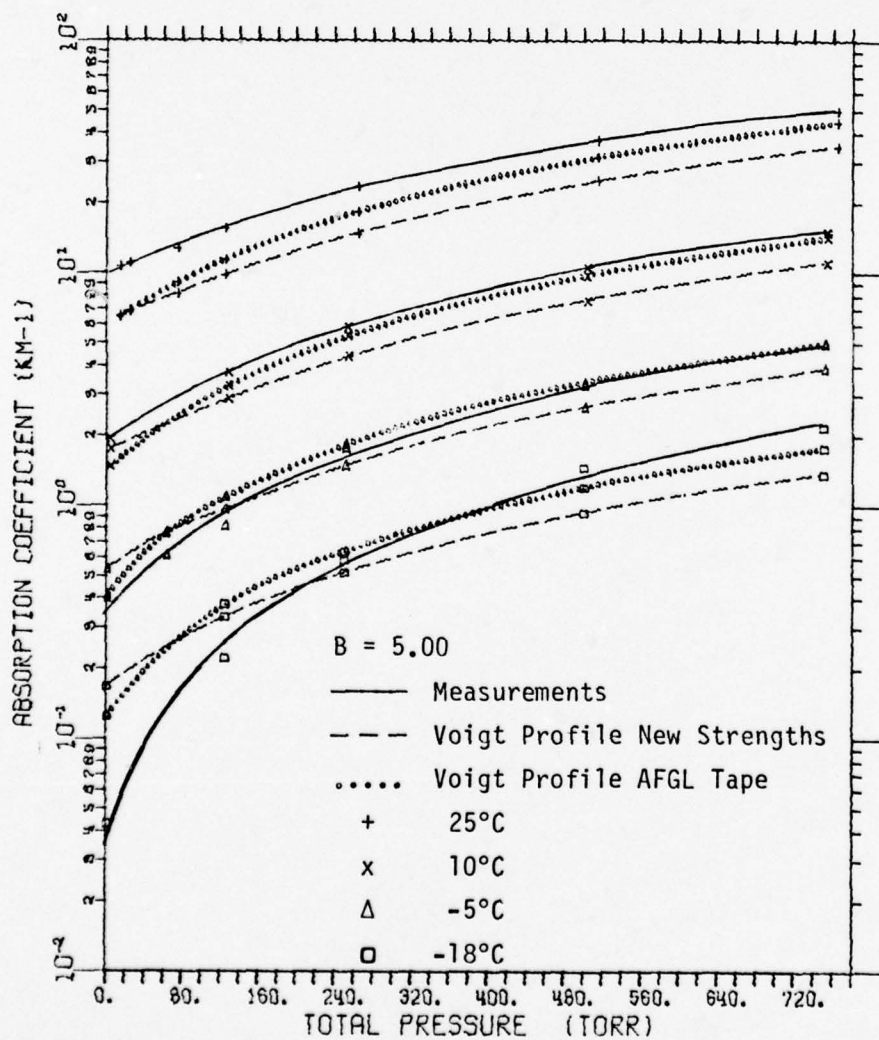


Figure 18. Measured absorption coefficients and calculated Voigt predictions for HF laser line P₁(7) using standard and modified AFGL line tabulations.

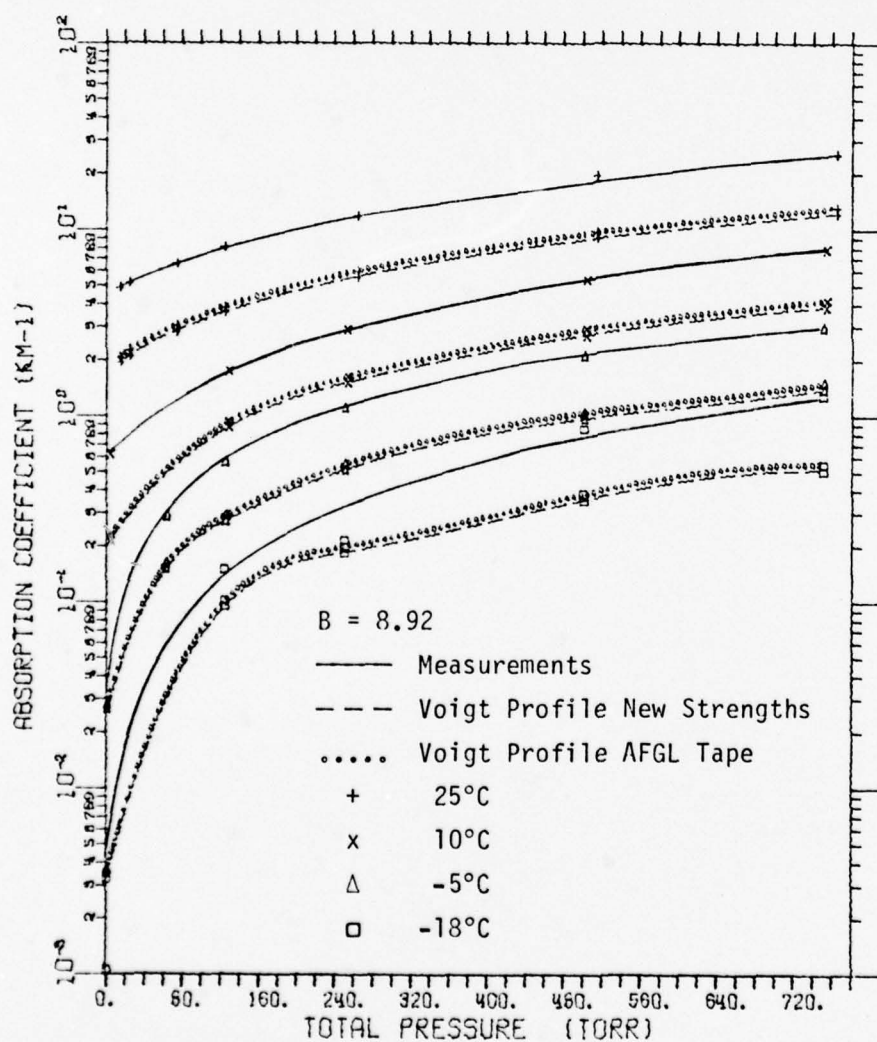


Figure 19. Measured absorption coefficients and calculated Voigt predictions for HF laser line $P_1(4)$ using standard and modified AFGL line tabulations.

CONTENTS

	<u>Page</u>
BACKGROUND	2
INTRODUCTION	3
EXPERIMENTAL APPROACH	4
MEASUREMENTS	18
LINE-BY-LINE CALCULATIONS	25
MEASURED AND CALCULATED COEFFICIENTS	33
DISCUSSION	49
CALCULATED ABSORPTION COEFFICIENTS FOR MODEL ATMOSPHERES	52
CONCLUSION	59
APPENDIX A. METHODS OF EVALUATION FOR THE SUPER- VOIGT LINE PROFILE	62
APPENDIX B. MEASURED AND CALCULATED ABSORPTION COEFFICIENTS FOR SELECTED HF LASER LINES	72
REFERENCES	83

BACKGROUND

The hydrogen fluoride (HF) laser is severely attenuated by water vapor in the atmosphere. However, its high power efficiency and relatively short infrared wavelength (compared to other chemical lasers) results in good focusing quality, making it ideally suited for use under atmospheric conditions of very low water vapor content. These conditions prevail in the upper atmosphere where the HF laser can be used as a high energy laser weapon or remote sensor. Because of this, use of the HF laser is of greater concern to the Air Force than the Army. Due to the interest in the HF laser, the Air Force Weapons Laboratory (AFWL) and the Atmospheric Sciences Laboratory (ASL) undertook a joint effort to parametrically measure the temperature and pressure dependence of water vapor absorption for HF laser radiation. The results of this investigation provide a new data base from which more accurate predictions can be made for high altitude (typically 12 to 18 km) absorption of HF laser radiation. Additionally, the resultant line shape as well as the self-to-foreign broadening coefficients shed new light on the understanding of the weak water vapor continuum absorption which persists throughout the 3-5 μ m atmospheric window.

The measurements contained in Part I of this report cover temperature and pressure regions corresponding to altitudes up to 7 km. In Part II lower temperatures will be used, and models for altitudes up to 12 km or higher will be verified.

INTRODUCTION

Obtaining accurate predictions for absorption of HF laser radiation in the upper atmosphere (12 to 18 km) is a complex task involving molecular absorption from water vapor (including H_2O and HDO isotopes), carbon dioxide and nitrous oxide. Tabulated values from the Air Force Geophysics Laboratory (AFGL) absorption line parameter compilation [1] can be used to calculate absorption coefficients for these species at the discrete laser wavelengths. However, pressure and temperature dependencies of the line parameters as well as the absorption line shapes must be known in order to make these calculations. The validity of these factors as well as the accuracy of the line parameter values themselves all enter into the accuracy of the absorption coefficient predictions. This report presents results of a parametric study of the water vapor absorption at selected HF laser lines. In addition, a limited effort to determine carbon dioxide absorption is also reported. The following sections present (a) descriptions of the experimental apparatus and approach, (b) the measurement parameters, (c) an in-depth comparison of the results with predictions, including line shape, broadening, and line parameter modifications, and (d) predictions, using the new data base and improved line shape, of transmission for an operational scenario. The culmination of this research, namely new predictions for absorption coefficients as a function of altitude, are given in Figures 24-30 for seven HF laser lines. The water vapor absorption in particular is summarized in the conclusion - the data being given in Appendix B.

EXPERIMENTAL APPROACH

In order to perform parametric temperature and pressure studies of the absorption of HF laser radiation by water vapor and other gases, a stable HF laser source and a longpath absorption cell are required. In the present study a longpath White cell is used which is temperature controllable from -18° to 25°C , in conjunction with an HF laser system, a data acquisition and reduction system, and several peripheral systems for creating a controlled cell atmosphere and water distillation.

The HF laser system consists of a Lumonics Model TEA-203 multigas laser employing transverse excitation of the lasing gas mixture which consists of SF_6 , H_2 , He and O_2 . Transverse excitation allows large quantities of energy to be dumped into this lasing gas mixture. The energy of the electrons in the plasma dissociates some of the SF_6 molecules with the resulting excited fluorine atoms combining with the H_2 to form HF molecules in excited vibrational states. Lasing occurs when the HF molecules make the transition to the next lower vibrational energy band. For HF only P branch lines ($\Delta J = +1$) with energy band transitions of $V=3 \rightarrow 2$, $V=2 \rightarrow 1$, and $V=1 \rightarrow 0$ generally occur. Pumping by transverse excitation subjects the lasing gas mixture to high current densities which results in the plasma discharge being unstable creating a condition known as bright arcing. The resulting high density plasma formed during

pumping absorbs some of the optical energy present in the cavity which in turn greatly reduces the energy output and limits the laser to pulsed operation. The He and O_2 in the lasing gas mixture are not necessary for the lasing action. O_2 is used to eliminate sulfur and fluorine compound deposits on the electrodes and discharge tube. Helium is added to minimize the possibility of an explosive H_2 - O_2 mixture.

The experimental setup for the Lumonics TEA-203 HF laser is shown in Figure 1. The laser has a 50-mm diameter calcium fluoride (CaF_2) lens with a centrally located 10-mm diameter gold-coated reflecting surface. Due to its unstable resonator mode of operation the laser produces a TEM-00 output beam which is donut-shaped in the near field. The rear reflector, a micrometer adjustable grating, provides a means for wavelength selection. The He-Ne laser beam is made coincident with the HF beam by using a flat, oval-shaped, mirror FM3 (see Figure 1) with a 6-mm diameter hole drilled through its center along the He-Ne optical axis. The donut-shaped near-field HF laser output beam is then centered on the hole in this mirror. The position is checked using a sheet of liquid crystal.

By inserting the lens, mirror and spectrum analyzer shown in the dashed box of Figure 1 into the beam the wavelength can be checked. In many instances the near-field beam consisted of two or three different single wavelength output beams. Multiple wavelength output can occur due to

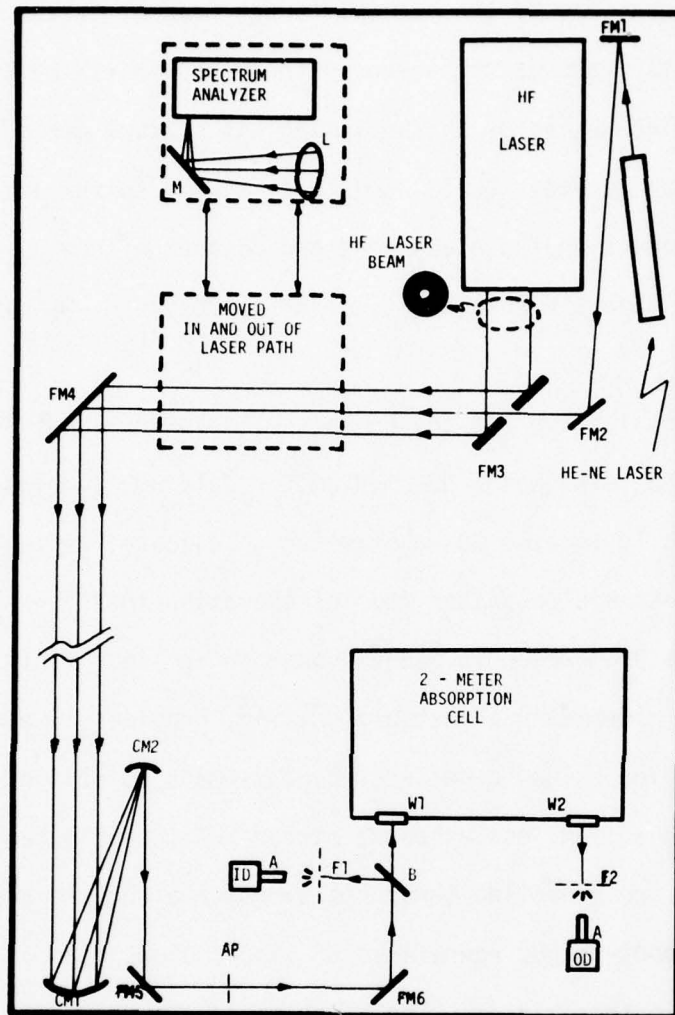


Figure 1. Experimental setup for conducting HF laser water vapor absorption experiments: FM1, FM2, FM4, FM5, FM6, and M, flat surface mirrors; FM3, special flat surface mirror with the central hole drilled along He-Ne axis; CM1 and CM2, collection and collimating spherically concave mirrors; B, 2-mm thick calcium fluoride beam splitter; F1 and F2, Teflon diffuse transmittance filters; AP, adjustable aperture; A, detector apertures; W1 and W2, 6-mm thick calcium fluoride cell windows; ID and OD, input and output indium antimonide detectors; and L, lens.

the close spacing of the HF wavelengths and the lack of sufficient dispersion due to the limited length of the laser cavity. It should be noted however that these undesired lines diverge quite rapidly from the central wavelength and are therefore no problem by the time they have travelled the distance of 12 m to the collection and collimation optics (see Figure 1).

Once wavelength selection is made the beam geometry of the HF laser output is checked. To do this a CaF_2 lens with focal length of 1 m is inserted into the beam just after reflection from mirror FM3 and either a liquid crystal sheet or a carbon block is used to observe the HF output pattern depending on output intensity for the particular wavelength. At this time the CaF_2 front reflector is adjusted by means of micrometer drives to correct the HF beam geometry so as to produce a donut-shaped output of uniform intensity in the near field.

Mirror FM3 is equipped with selsyn receivers attached to the mirror's micrometer drives. Selsyn transmitters located near the 2-m cell input window allow remote control positioning of the HF beam in order to keep it coincident with the He-Ne beam [2] (see Figure 2a).

After reflecting off FM4, both the He-Ne and HF beams travel a distance of 10 m and are collected by an 11-cm diameter 1-m focal length concave

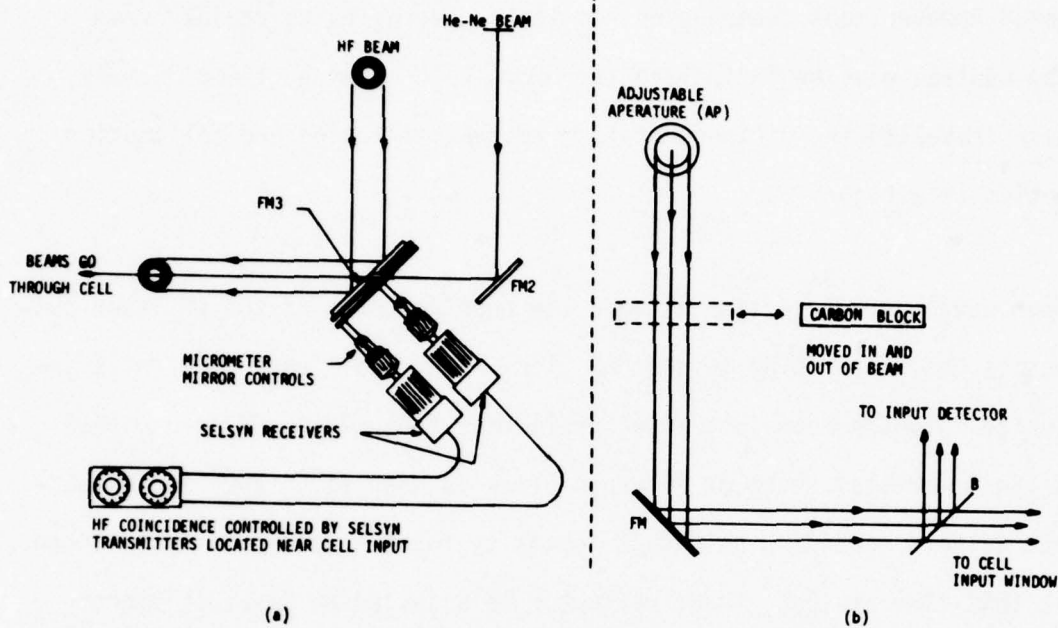


Figure 2. (a) Remote selsyn receivers attached to special mirror FM3 with the central hole drilled along He-Ne axis. (b) Location of carbon block insertion in order to adjust beam coincidence using selsyn transmitters.

mirror CM1 (see Figure 1). CM2 (a second concave mirror of 30-cm focus, 3-cm diameter) is used to collimate the beams for both laser sources. The HF beam, having only travelled a distance of 12 m from the laser cavity front optic to CM1, is unable to make the transition to the far field and the resultant beam after collimation has the appearance of a TEM-02 geometry (see Figure 3). Both beams then pass through the adjustable aperture (AP) shown in Figure 1. At this point, beam coincidence is checked by placing a carbon block in the beams' path between adjustable aperture (AP) and mirror FM6. Selsyn transmitters are then used to position the HF beam. A 2-mm thick CaF_2 optical flat (B) is used to split a portion of both beams to the cell input (reference) detector (ID). The remaining portion of both beams then passes through a 6-mm thick, 50-mm diameter CaF_2 window (W1) and into the longpath White cell. Figure 4 shows the details of the White cell optical path. The exciting beam then emerges from the cell output window (W2, also 6-mm CaF_2) and passes to the cell output (sample) detector (OD). Liquid nitrogen cooled indium antimonide (InSb) detectors are used for both ID and OD.

Teflon membrane filters (F1 and F2 in Figure 1) are placed in front of the input and output detectors. Millipore type LSWP04700 Teflon filters with a pore size of $5\mu\text{m}$ are used to diffuse the beam. Room air turbulence as well as mechanical vibrations and temperature variations affecting the optics external to the cell cause beam jitter and wander on

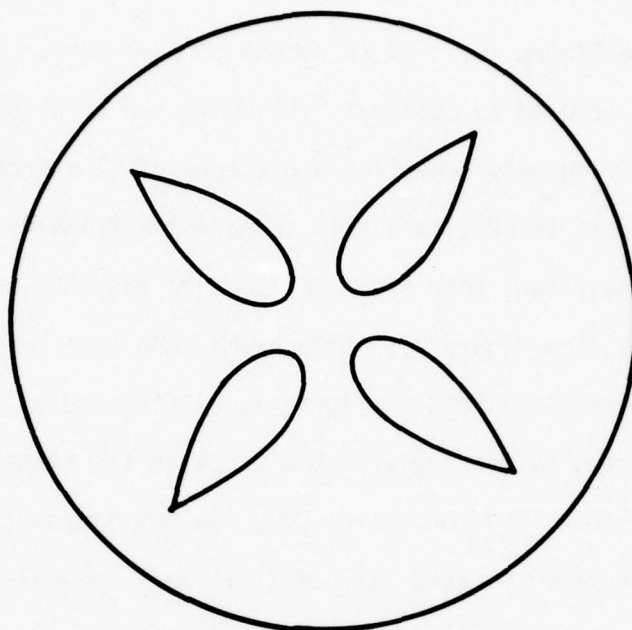


Figure 3. Collimated HF beam geometry.

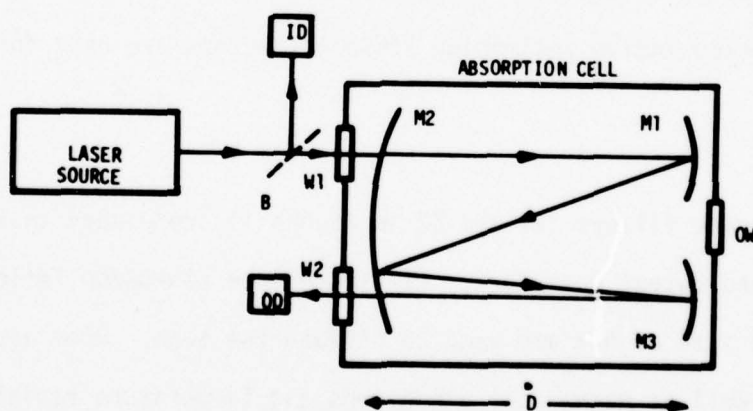


Figure 4. Conventional "White type" absorption cell experimental setup: B, beam splitter; W1 and W2, cell windows; OW, observation window; ID and OD, input and output detector systems; M1, M2, and M3, spherically concave cell mirrors; and D, separation distance between cell mirrors.

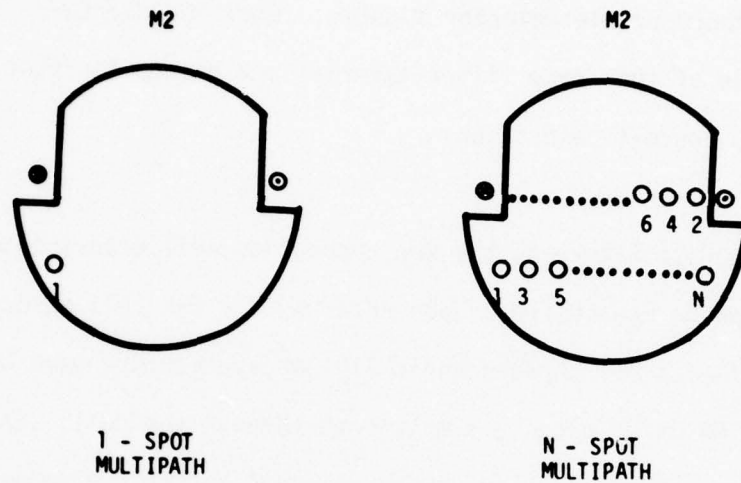


Figure 5. Views of mirror M2 as seen from the observation window OW for a 1-spot (a) and an N-spot (b) multipath; numbered circles, images of laser source on mirror surface; circle with central dot, laser beam entering cell; and circle with "X," laser beam exiting cell.

the detectors and in turn drastically affect the output signal levels. By using diffusion filters these effects are minimized since the detectors are then looking at an averaged intensity over a larger area resulting in reproducible detector signals. Limiting apertures (A) with backings made of this same filter material are placed in front of the detectors to prevent saturation.

Referring back to Figure 4, the 2-m absorption cell experimental setup used will now be considered. Upon entering the 2-m cell through W1, the beam reflects off three spherically concave mirrors seen here as M1, M2, and M3 which produce a multipath through the cell. Each of these mirrors has a radius of curvature equal to the 2 m separation distance D. The number of passes which both beams make through the cell can be determined by looking through observation window (OW) and physically counting the number of images on M2. Figure 5 shows both a 1-spot and an N-spot multipath pattern on M2 as viewed from OW. Here the N-spot multipath has a pathlength equal to $2(N+1)D$.

The usual method for obtaining absorption coefficients for the particular absorbing gas of interest is to obtain relative transmittance values for two cell conditions - one with a nonabsorbing atmosphere and the other with the absorbing gas. Both these measurements are made at the longest possible multipath. Absolute transmittance, the ratio of these two relative transmittance measurements, yields the absorption coefficient for the absorbing medium.

A new technique called path differencing (described elsewhere [3] in detail) is used for the present measurements in order to provide the cell's single beam system with the advantage of time independence like that found in spectrophotometers which have a double-beam calibration scheme. Basically path differencing uses a method of rapid changes in pathlength between two different multipath lengths. Path differencing minimizes time dependencies of the measurement which are caused by such changes as temperature, vibration, and beam wander.

Pathlength changes in the cell are accomplished by means of vacuum micrometer drives located on the same end of the cell as the observation window. Both M1 and M3 of Figure 4 are equipped with these micrometer drives allowing both horizontal and vertical plane adjustment. M2 is mounted in a fixed position. Once M1 is properly positioned so as to place the coincident beams on M2 as shown in Figure 5a, an N-spot multipath (Figure 5b) can be obtained by simply adjusting M3. Repositioning of the cell output beam is routinely possible to within ± 1 mm between a 41-spot multipath (168-m pathlength) and a 3-spot multipath (16-m pathlength) in 1 minute. After the multipath is established, final cell output alignment is accomplished by positioning the output He-Ne defraction pattern on the cross hairs of Teflon filter F2. A 3-spot multipath is used for the minimum pathlength because of limitations in the micrometer drive of mirror M3. Finally, it should be noted that the most important part of the optical alignment process is the reproducible positioning of the #1-spot on mirror M2. If this is not done accurately, the multipath spots will not occupy the same positions on the surfaces of each of the 3-cell mirrors. Use of a

collimated input beam reduces the effect of imperfections in the mirror surfaces; but unless consistent realignment is performed large discrepancies in cell transmission can occur due to different values for overall mirror reflectance, especially for longpath differences.

The signal analyzing system used for the input and output detector signals is described in detail in reference 4 and is shown in Figure 6. HF laser pulses are typically submicrosecond in duration with a frequency of from 0.1 to 0.3 Hz depending on charging voltage. Both indium antimonide detectors have output signals which follow the rise time of the laser pulses with a decay time of several microseconds. The ratio of the detector's pulse heights is then used to determine transmittance. The output signals from both detectors are fed into Ortec 450 amplifiers which bring the signals to a level between the 2 and 10 volts required for digitization. The usual output voltage level is set at 7 volts with a ± 1 volt fluctuation caused by variations in the laser's output intensity. The cell input detector signal is sent through an Ortec 427A delay which matches the optical delay experienced as the beam propagates through the absorption cell. Both detector signals are fed into 14-bit Hewlett-Packard 5416B analog-to-digital converters. These two digitized signals are displayed as a single point on a digital xy-oscilloscope (see Figure 7) and analyzed by computer programs. This real-time display of the two detector signals enables both detection and correction of nonlinearities and typical alignment problems during the measurements.

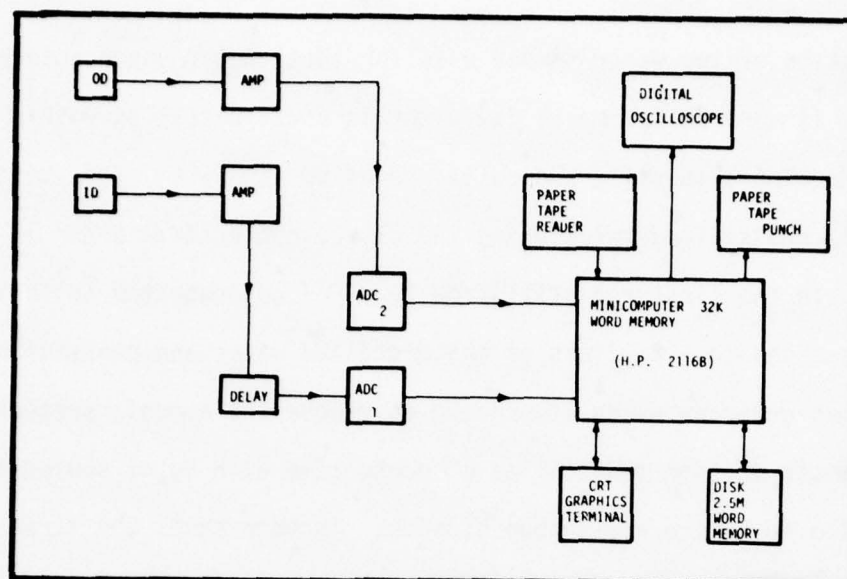


Figure 6. Block diagram of minicomputer analyzer system.

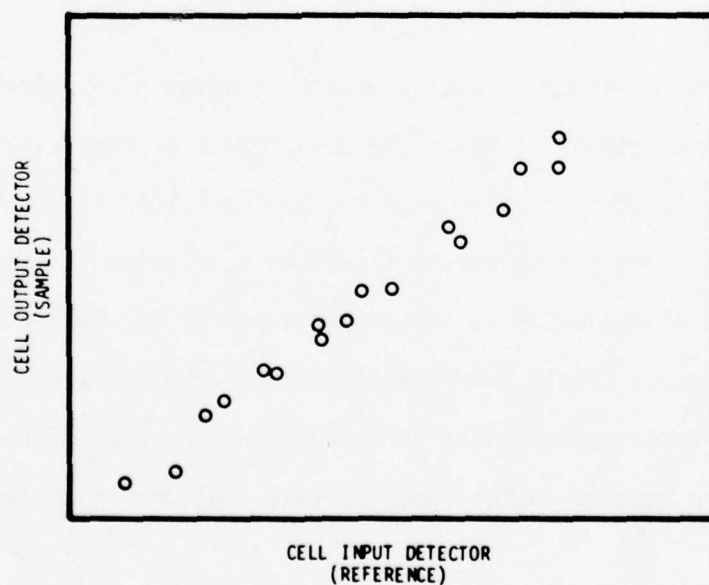


Figure 7. Display as seen on digital XY oscilloscope illustrating proper alignment conditions for short pathlength case.

Preparation of the water sample used for these water vapor absorption studies is done as follows:* The water is first distilled with a Barnstead Model A-1115 still and collected at 90° to 95°C. This distilled water is redistilled twice using the closed-cycle still shown in Figure 8. In the first redistillation 20 ml of concentrated sulfuric acid is added to 1.2 liters of the distilled water and redistillation performed under an argon atmosphere to remove any ammonia present. This sample is then redistilled a second time with 5g of sodium hydroxide added to remove any carbon dioxide. In both cases the first 50 ml of distillate is discarded, 750 and 500 ml, respectively, of the samples are collected with the remaining residue in the boiling flask discarded. Between distillations the boiling flask is flushed with singularly distilled water and baked dry. The final sample is stored in a dual-ground glass seal flask under argon.

The desired water vapor partial pressure is obtained by slowly bleeding in the required amount of specially prepared water sample through a vacuum valve located on the top of the 2-m cell (see Figure 9). The water sample is held in a sealed titration tube which is attached to a 7-cm conflat flange which is in turn attached to the vacuum valve. To keep the water sample from freezing as it is evaporated into the evacuated 2-m cell, the vacuum valve and lower portion of the titration tube are heated. Water vapor partial pressure is monitored using

**This distillation process was developed by E. J. Perry and C. W. Bruce of the ASL, White Sands Missile Range, NM 88002, in an unpublished report to CPT T. Walker of the AFWL.*

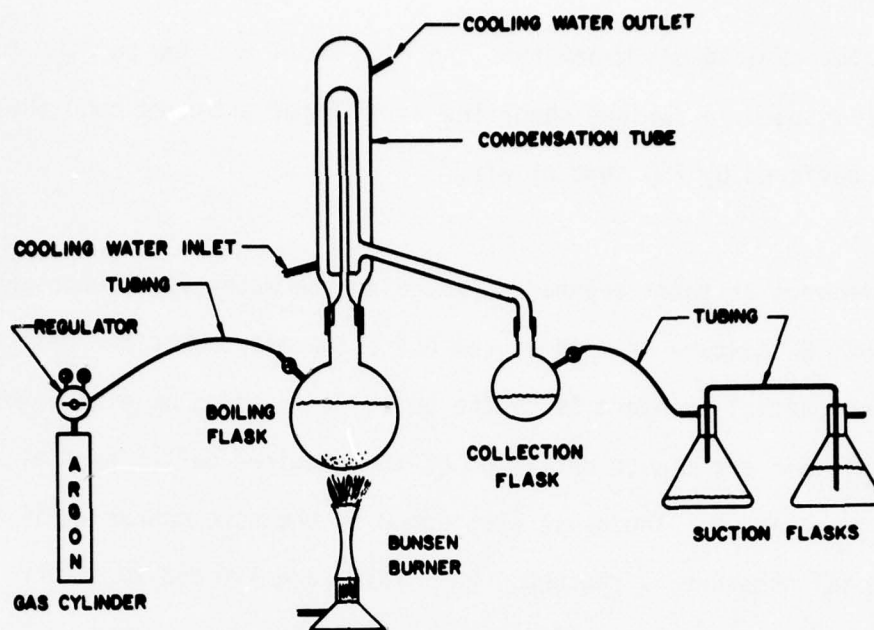


Figure 8. Closed cycle distillation apparatus.

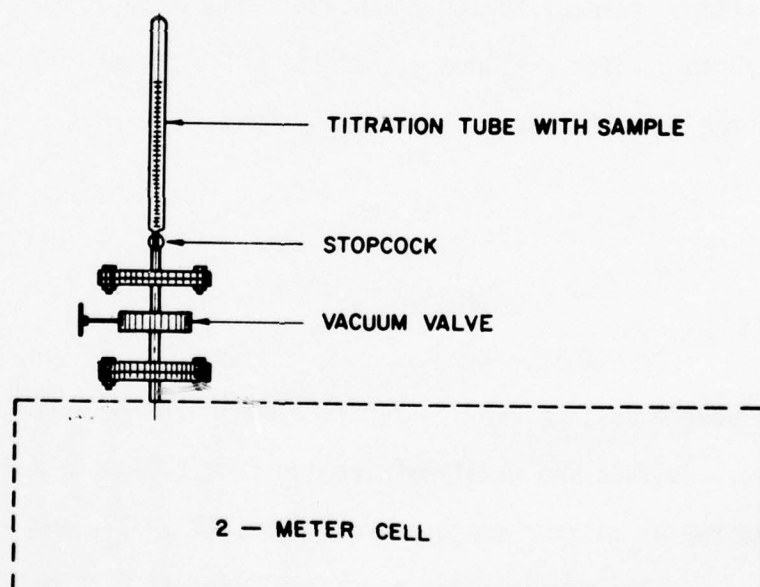


Figure 9. 2-meter absorption cell water inlet tube assembly.

a Datanetrics capacitance manometer. An EG&G Model 880 dew point hygrometer is used to further check the water vapor pressure once the sample is buffered by 750 torr of air.

For measurements at total pressures exceeding the water vapor pressure a 20% O₂-80% N₂ mixture is used as the buffering gas. Once the desired water vapor partial pressure is in the cell, O₂ is added at a rate not exceeding 4 torr per minute until 20% of the required buffer partial pressure is obtained. The N₂ is then added in the same manner until the desired total pressure is reached. Fill rates are limited to 4 torr per minute since for greater fill rates some of the water vapor will begin to condense. Standard equilibration is typically 2 hours for fill rates less than or equal to 4 torr per minute although most atmospheres are allowed to equilibrate overnight. Again capacitance manometers are used to monitor pressure within the cell. Figure 10 is a schematic of the 2-m cell vacuum and fill systems.

MEASUREMENTS

Measurements were made in a 2-m, temperature controllable White cell. Seven HF lines covering the wavelength region from 2.64 μ m to 2.91 μ m were observed for up to four temperatures: 25°, 10°, -5°, and -18°C. Limited data were also obtained for two other lines at 25°C only. Water vapor pressure at the temperatures used corresponded to approximately 50% relative humidity.

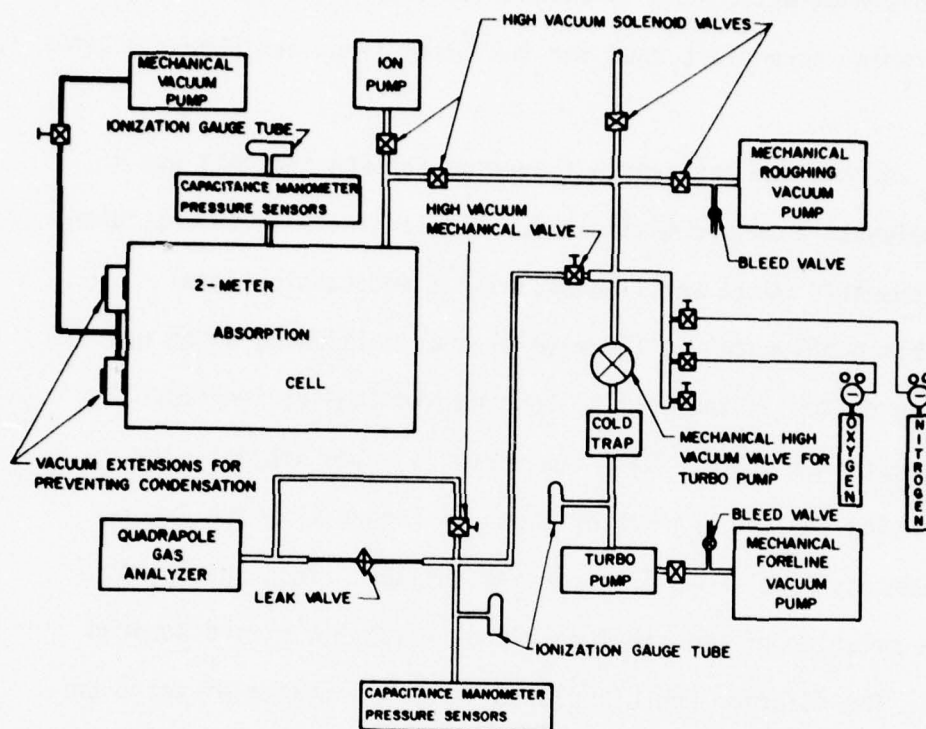


Figure 10. 2-meter absorption cell vacuum system.

An 80-20 mixture of N_2-O_2 was added to the water vapor concentrations for selected partial pressure values between 0 and 750 torr. In addition, two additional water vapor pressures were used for the 25°C condition. Measurement parameters used for the laser lines are shown in Table 1.

In all cases the minimum pathlength traversed through the cell was 16 m (corresponding to a 3-spot multipath). The long pathlength was taken as large as possible while still maintaining a detectable signal. Maximum useable pathlength was 168-m (a 41-spot multipath) which was limited by the optics in the cell.* Long pathlengths varied from 32 m (7-spot multipath) to 168 m. Cell temperatures below ambient were achieved by using the cooling system shown in Figure 11 which incorporated an Edmunds Model CC-3-A commercial chiller. This unit continually kept a solution of 60% ethylene glycol - 40% H_2O at the desired temperature. The solution was circulated through a system of veins on the exterior surface of the cell to provide the cooling. Temperature stability, once the desired low temperature was reached, was maintained by thermostatic control of the coolant being circulated. A 10-cm thick

**At pathlengths greater than 168 m (41-spot multipath) the He-Ne alignment laser diffraction pattern became difficult to observe making alignment on the cross hairs of the output detector filter difficult. In addition, at pathlengths of 182 m (a 45-spot multipath) clipping of the output beam occurred.*

TABLE 1
MEASUREMENT PARAMETERS FOR HF ABSORPTION

Laser Line	Temperature °C	Water Vapor Pressure (torr)	80-20 N ₂ -O ₂ Buffer Pressure														
			0	10.7	15	20	60.7	62.5	65	70	110.7	115	120	125	250	500	750
P ₁ (4), P ₁ (6), P ₁ (7), P ₂ (5), P ₂ (6) & P ₂ (7)	25	14.3	X	X			+X			X				X	X	+X	
	25	10.0			X				X		X						
	25	5.0				X					X						
	10	4.5	X									X	X	X	X	X	
	-5	1.5	X						X			X	X	X	X	X	
	-18	0.5	X						*			X	X	X	X	X	
<hr/>																	
P ₂ (8)	25	14.3	X	X			X			X				X	X	X	
only	10	4.5	X									X	X	X	X	X	

*This case done for laser line P₁(6) only.

+This case done for laser lines P₁(8) and P₃(5).

NOTE: Only the two indicated cases for P₁(8) and P₃(5) were done.

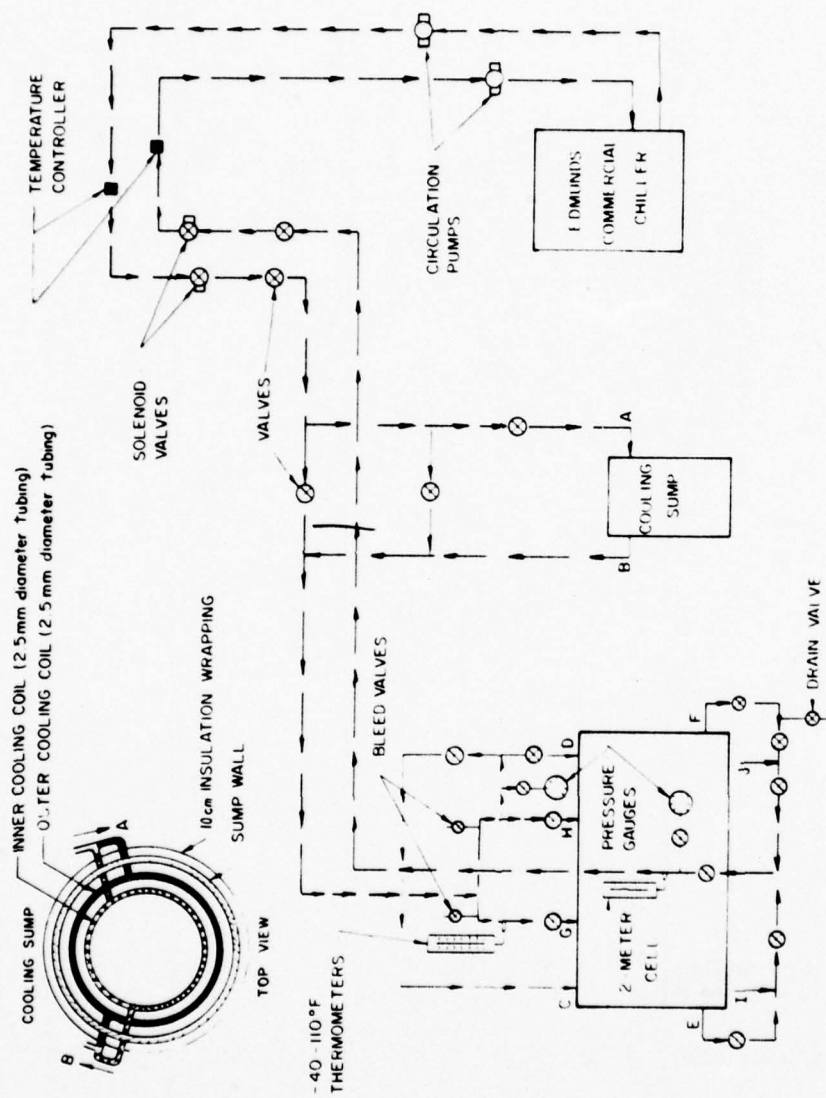


Figure 11. 2-meter absorption cell cooling system.

fiberglass insulation wrapping on the cell ensured temperature stability. Vacuum extensions were added to the cell windows to prevent condensation and icing. For the -18°C temperature case it was necessary to use a slightly different method for cooling due to compressor limitations on the Edmunds chiller. The chiller was used to bring the cell temperature to -5°C and at this point was turned off. The system circulation pumps were kept running and the remaining 13°C drop obtained by use of a cooling sump (which contained 20 gallons of an ethylene glycol - H_2O mixture in a 60-40 ratio) to which dry ice was added as needed to bring and maintain the sump temperature to the desired level (see Figure 11). The sump itself consisted of a well insulated cylindrical tank with two inside circumferential wraps of 1.3-cm tubing running about $2/3$ of the way up the side of the 1-m high tank (one coil wrap inside the other). Some 700 kilograms of dry ice was required to drop and keep the cell temperature stable at -18°C for the 32-hour data gathering period.

During this 32-hour data acquisition period it was noted that HF laser lines $P_1(6)$, $P_1(7)$, and $P_2(5)$ showed rather substantial drops in laser output power as seen by both cell input and output detectors. This was caused by the increase in CO_2 content in the laboratory atmosphere from the dry ice boiloff. This CO_2 absorption prompted an additional study of CO_2 absorption for these three lines. These measurements were made for the conditions shown in Table 2.

TABLE 2
MEASUREMENT PARAMETERS FOR CO₂ ABSORPTION

P _{total} (torr)	P _{CO₂} (torr)	Temp (K)
75	0.434	298
75	3.000	298
760	0.434	298

A comparison was also made to determine the effects of oxygen broadening in relation to the standard 80-20, N_2-O_2 broadening. This was done for HF lines $P_1(4)$, $P_1(6)$, $P_1(7)$, $P_2(5)$, and $P_2(6)$ for 14.3 torr H_2O buffered to 75 torr total pressure with pure oxygen at 25°C.

LINE-BY-LINE CALCULATIONS

Of the methods available for calculating atmospheric transmission, only line-by-line procedures have sufficient spectral resolution to be applicable when computing the attenuation of HF laser radiation. These procedures evaluate the total absorption coefficient at a given frequency (ν) by summing the contributions of all significant spectral lines in the vicinity of this frequency. In general, the absorption coefficient of a single absorption line is given by

$$k(\nu) = Sx f(\gamma, \nu - \nu_0) \quad (1)$$

where S is the line strength, x the concentration of the absorbing species, and $f(\gamma, \nu - \nu_0)$ a shape factor defining the line profile appropriate for the particular broadening conditions. At pressures above approximately 0.1 atmospheres pressure broadening is dominant and the line shape is given by the Lorentz profile: [5]

$$f_L(\gamma_L, \nu - \nu_0) = \frac{\gamma_L}{\pi[(\nu - \nu_0)^2 + \gamma_L^2]} \quad (2)$$

where γ_L is the Lorentz half width of the spectral line and ν_0 the line center frequency (cm^{-1}). At very low pressures collisional broadening is negligible but the motions of the absorbing molecules give rise to Doppler effects. Under these circumstances the line is Doppler broadened and the shape factor is given by: [6]

$$f_D(\gamma_D, \nu - \nu_0) = \sqrt{\frac{\ln 2}{\gamma_D^2 \pi}} \exp [-(\ln 2)(\nu - \nu_0)^2 / \gamma_D^2] \quad (3)$$

where ν_0 is again the line center frequency and γ_D is the Doppler half width. At intermediate pressures, such as those encountered in upper atmospheric work, both Doppler and pressure broadening contribute. In this case the resulting shape factor is the Voigt profile given by the convolution of the separate Doppler and Lorentz profiles. It may be shown that this convolution is given by: [6]

$$f_V(\gamma_L, \gamma_D, \nu - \nu_0) = \frac{\gamma_L \sqrt{\ln 2}}{\pi \gamma_D} \int_{-\infty}^{\infty} \frac{\exp(-t^2) dt}{y^2 + (z - t)^2} \quad (4)$$

where

$$y = \frac{\gamma_L}{\gamma_D} \sqrt{\ln 2}$$

and

$$z = \frac{(\nu - \nu_0)}{\gamma_D} \sqrt{\ln 2} .$$

Since this profile reduces to the proper limiting shape (Lorentz or Doppler) under the appropriate conditions, it may be used in all pressure regimes except where collisional narrowing is important, although its evaluation is more difficult than either Eq. (2) or Eq. (3).*

With any of the above shape factors, the total absorption coefficient at frequency ν (neglecting line overlap contributions) is given by the sum of the absorption coefficients of all significant spectral lines in the vicinity of ν or:

$$K(\nu) = x \sum_i S_i f(\gamma_i, \nu - \nu_{0i}) . \quad (5)$$

Generally the range over which this sum must be taken in order to insure an accurate evaluation of $K(\nu)$ is defined in terms of the distance

*For a discussion of the computational methods used to evaluate the Voigt profile in the present study see reference 7.

$(\nu - \nu_0)_{\max}$ that a strong line must be separated from the point of computation for its contributions to the absorption coefficient to be negligible. Once $(\nu - \nu_0)_{\max}$ is determined the sum is taken over all spectral lines for which $|\nu - \nu_0| \leq (\nu - \nu_0)_{\max}$.

In carrying out the sum in Eq. (5) the line strengths (S_i), half widths (γ_i), and positions (ν_{0i}) must be known for all contributing spectral lines. In the present work these parameters have been taken from the Air Force Geophysics Laboratory line tabulation [1] with some modifications being made based on the recent work of Flaud and Camy-Peyret [8]. Since the tabulated strengths are those appropriate for 296 K while the line widths are those for air broadening at this temperature, corrections are required to modify these strengths and widths before calculations can be compared to the experimental data.

For the line strengths the temperature variation is taken as:

$$S(T) = S(T_0) \frac{Q_R(T_0) Q_V(T_0)}{Q_R(T) Q_V(T)} \exp \left[- \frac{hc E''}{k} \left(\frac{1}{T} - \frac{1}{T_0} \right) \right] \quad (6)$$

where h is Planck's constant, c the speed of light, k Boltzmann's constant, E'' the lower state energy of the transition, Q_R the rotational partition function, and Q_V the vibrational partition function. The ratio of the rotational partition functions at temperatures T_0 and T may be shown to be [9]

$$\frac{Q_R(T_0)}{Q_R(T)} = \left(\frac{T_0}{T}\right)^j \quad (7)$$

where $j=1$ for diatomic or linear polyatomic molecules and $j=3/2$ for symmetric, spherical, and asymmetric top molecules. The vibrational partition function is more difficult to evaluate but a good approximation at atmospheric temperatures is given by the harmonic oscillator approximation:

$$Q_V(T) = \prod_i [1 - \exp(-\omega_i hc/kT)]^{-d_i} \quad (8)$$

where ω_i is the frequency of the i^{th} normal vibration referenced to the ground state level and d_i is the degeneracy of this level. This expression has been used to evaluate the ratio of vibrational partition functions in the present work. For the line half widths the temperature dependence is assumed to be:

$$\gamma(T) = \gamma(T_0)(T_0/T)^m \quad (9)$$

where kinetic theory predicts m to be $1/2$ assuming constant collision diameters. The value of $1/2$ has been used here for all molecules except H_2O for which the average value of 0.62 , as determined by Benedict [10], has been used. Since the half widths in the AFGL tabulation are air broadened values, self broadening has been taken into account using

$$\gamma = \gamma_{\text{air}}(P_f + BP_s) \quad (10)$$

where P_f is the partial pressure of the foreign (buffer) gas, P_s the partial pressure of the absorbing species, and B the self broadening coefficient normally taken as 5.0 for water vapor [11].

In the present study B -values have been determined in the vicinity of each laser line using the experimental data. If the Lorentz line shape of Eq. (2) is assumed, then in the wings of such a line where $(\nu - \nu_0) \gg \gamma_L$ and

$$k(\nu) \approx Sx \gamma_L / \pi(\nu - \nu_0)^2 .$$

Upon substituting Eq. (10) for the half width and expressing the density x in terms of the absorbing species partial pressure P_s and the absolute temperature T , this expression becomes:

$$k(\nu) \approx \frac{S \gamma_{\text{air}} P_s (P_f + BP_s)}{T \pi (\nu - \nu_0)^2} 7.34 \times 10^{26} .$$

The total absorption coefficient at a given laser line is then given by:

$$K(\nu) = P_s (P_f + BP_s) \frac{7.34 \times 10^{26}}{\pi T} \sum_i \frac{S_i \gamma_{\text{air}i}}{(\nu - \nu_{0i})^2} \quad (11)$$

where the sum is a constant for a given laser line at a given temperature. For each laser line the absorption coefficient was measured at 25°C with constant total pressure and varying water vapor partial pressures. Consequently taking the foreign gas pressure P_f as $(P_{total} - P_s)$ Eq. (11) gives:

$$K(\nu) = \text{CONST.} [P_s P_{total} + (B - 1)P_s^2] \quad (12)$$

or

$$K(\nu) = aP_s + bP_s^2 . \quad (13)$$

A least squares fit of Eq. (13) to the experimental data then yielded the self broadening coefficient B in terms of the fit parameters b and a giving:

$$B = P_{total}(b/a) + 1 .$$

An example of this procedure is shown in Figure 12 for laser line $P_1(6)$. The assumption inherent in this determination of B is that the absorption coefficient is dominated by far wings of lines or more explicitly that

$$[\gamma/(\nu - \nu_0)]^2 \ll 1 .$$

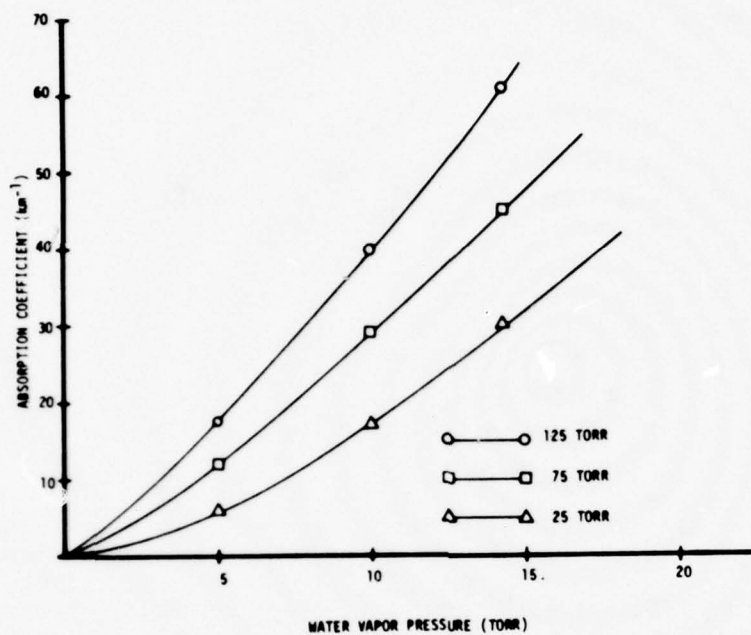


Figure 12. Absorption coefficient for laser line $P_1(6)$ plotted against water vapor partial pressure. Fits to these curves were used to evaluate broadening parameter B .

When this condition is satisfied, Eq. (12) is applicable and $K(\nu)$ should be linear in P_{total} for constant P_s . This was found to be true for all laser lines at 25°C for buffer pressures up to approximately 250 torr as shown in Figure 13 for laser line $P_1(6)$.

MEASURED AND CALCULATED COEFFICIENTS

Using the procedures outlined above the self broadening coefficients were determined in the vicinity of each of the HF laser lines giving the values shown in Table 3. These values were used in conjunction with the Voigt profile and the line parameters of the AFGL tabulation to calculate absorption coefficients at the laser lines for the experimental measurement conditions. Comparisons of the measured and calculated values, representative examples of which are shown in Figures 14 and 15, indicated excellent agreement for laser lines $P_1(6)$ and $P_2(6)$ while the calculated values for the other laser lines were consistently low. Two possible sources of error could account for these discrepancies: (1) errors in the line strengths, positions, or widths in the AFGL tabulation and (2) deviations from the assumed spectral line shapes especially in the far wings of the lines.

Since the line strengths for water vapor in the AFGL tabulation are values calculated by Benedict in which centrifugal distortion was

TABLE 3
SELF-BROADENING COEFFICIENTS B FOR
SELECTED HF LASER LINES AT 25°C

Laser Line	Frequency (cm^{-1})	Self-Broadening Coefficient B (Dimensionless)
P ₁ (4)	3788.2253	8.92
P ₁ (6)	3693.4226	4.34
P ₁ (7)	3644.1454	5.00
P ₂ (5)	3577.5002	6.30
P ₂ (6)	3531.1747	4.82
P ₂ (7)	3483.6522	8.20
P ₂ (8)	3434.9994	5.00

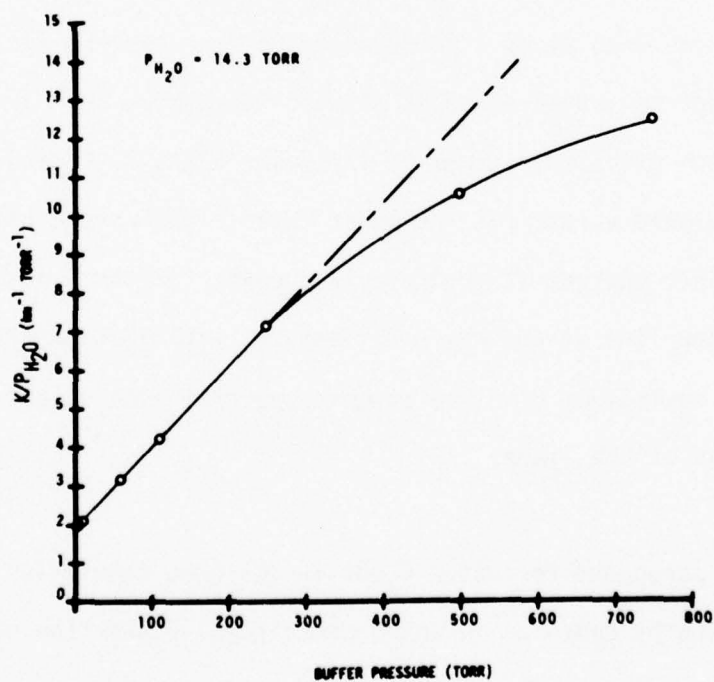


Figure 13. $K/P_{\text{H}_2\text{O}}$ vs buffer pressure for HF laser line P₁(6) at 25°C.
Linear region indicates far wing dominated regime.

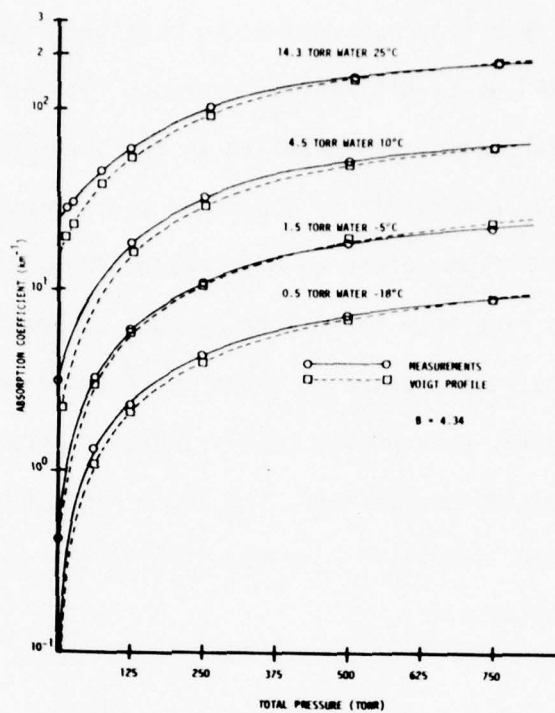


Figure 14. Measured and calculated absorption coefficients for laser line $P_1(6)$.

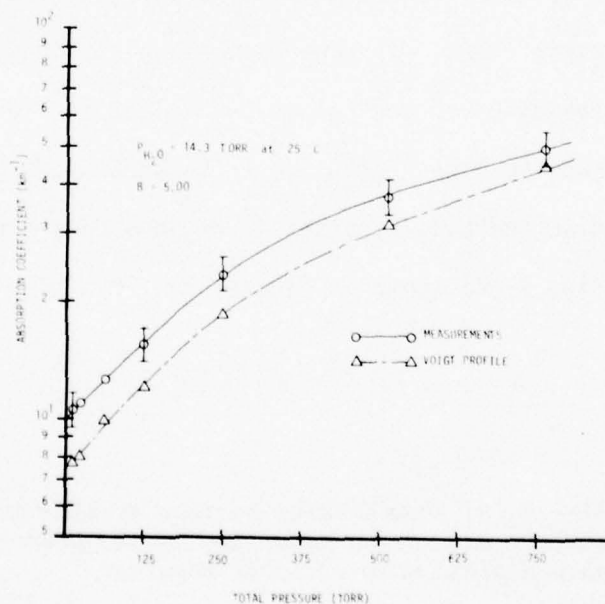


Figure 15. Measured values and Voigt predictions for HF laser line $P_1(7)$.

accounted for but ΔK effect and resonances have been ignored, these line strengths could be significantly in error. To minimize these errors, the AFGL tabulation was modified in the vicinity of laser lines $P_1(4)$, $P_1(7)$, $P_2(5)$, and $P_2(7)^*$ by inserting the strengths and lower state energies for 1H_2 16O from reference 8 in which all of the resonance and distortion effects have been taken into account at least in an approximate manner. Calculations based on these new tabulations, shown in Figures 16 through 19, gave substantially improved agreement between observed and calculated coefficients for laser lines $P_2(5)$ and $P_2(7)$; poorer agreement for line $P_1(7)$; and essentially the same results as the old strengths for line $P_1(4)$.

To determine the origin of the remaining discrepancies, plots were generated which showed not only the total absorption coefficient in the vicinity of a laser frequency but also the contributions of the individual spectral lines. In general these plots indicated good agreement between observed and calculated values for regions dominated by near wings such as lines $P_1(6)$ and $P_2(5)$ shown in Figures 20 and 21, while serious discrepancies resulted in regions dominated by far wings such as laser line $P_1(7)$ shown in Figure 22. This behavior was indicative

**The data for line $P_2(8)$ showed large scatter so that analysis of this line was impossible. Data being generated at the present time using spectrophones should yield more reliable results.*

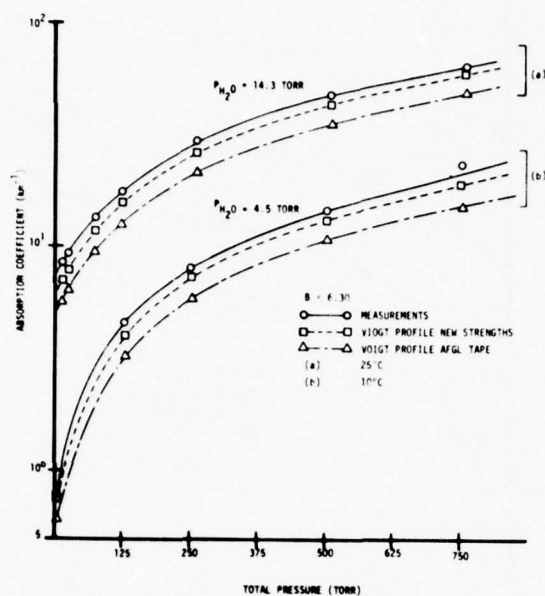


Figure 16. Voigt and super-Voigt predictions for HF laser line $P_2(5)$ using the AFGL and modified line tabulations.

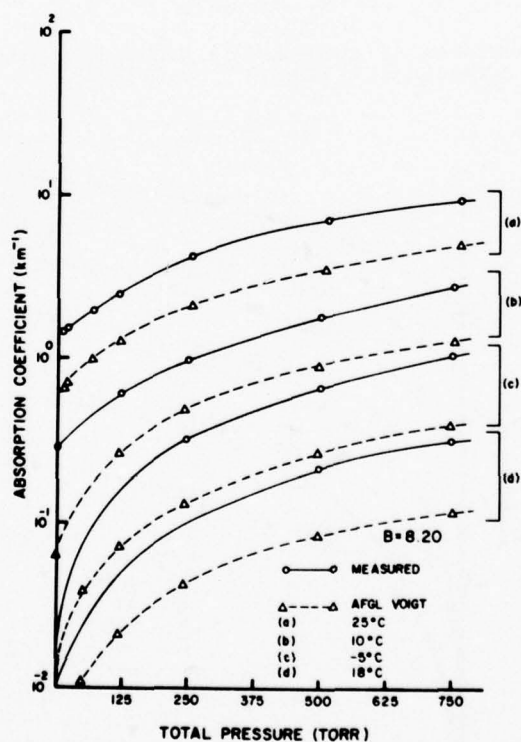


Figure 17. Measured and calculated Voigt absorption coefficients for laser line $P_2(7)$ using AFGL tabulation.

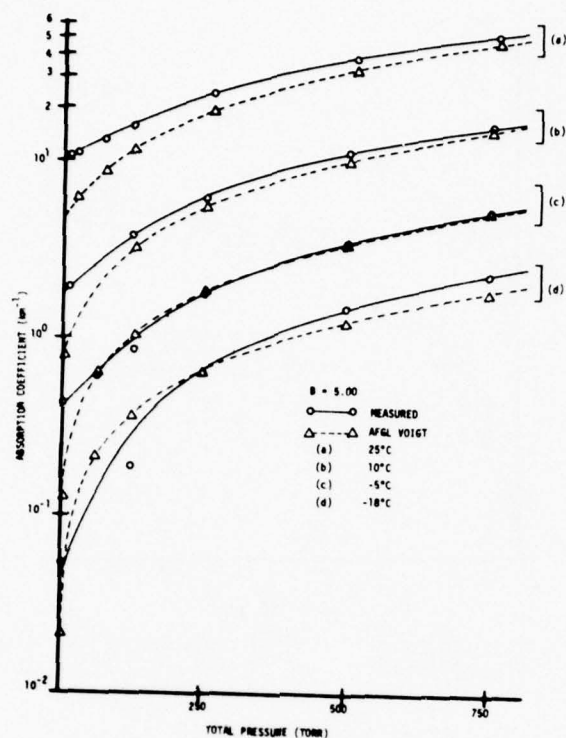


Figure 18. Measured and calculated Voigt absorption coefficients for laser line $P_1(7)$ using AFGL tabulation.

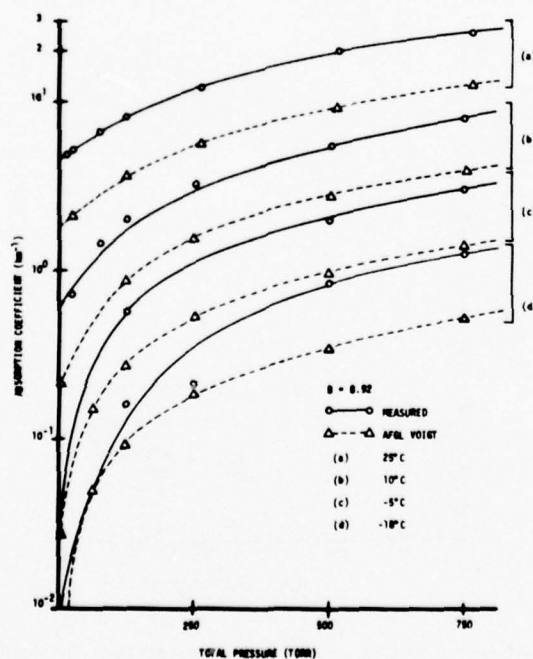


Figure 19. Measured and calculated Voigt absorption coefficients for laser line $P_1(4)$ using AFGL tabulation.

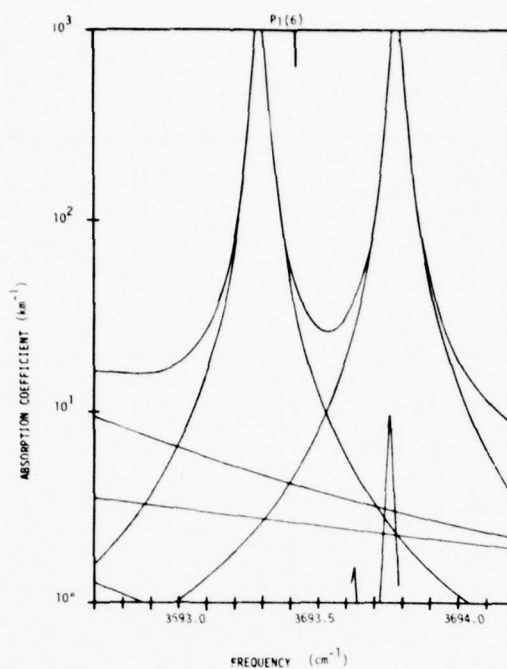


Figure 20. Absorption lines contributing to the total absorption at HF laser line $P_1(6)$ (shows near wing dominance).

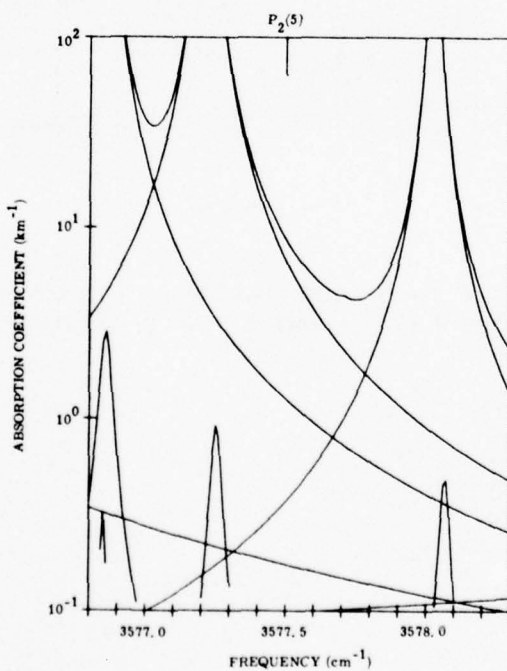


Figure 21. Absorption lines contributing to the total absorption at HF laser line $P_2(5)$ (shows near wing dominance).

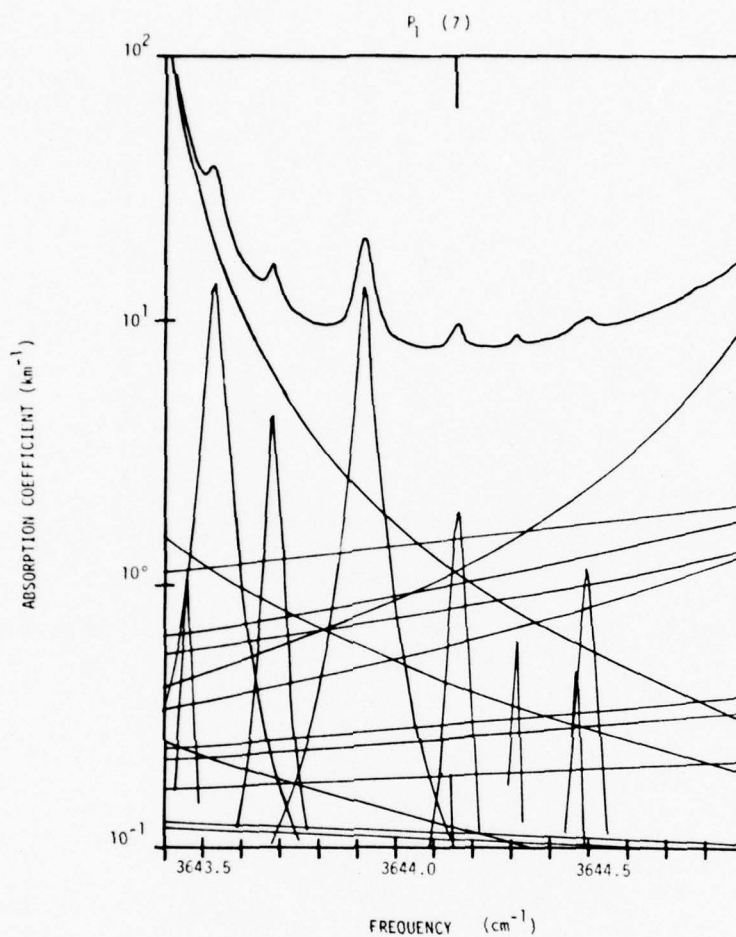


Figure 22. Absorption lines contributing to the total absorption at HF laser line $P_1(7)$ (shows far wing dominance).

of a deviation from the assumed line shape in the far wings of the absorption lines and in fact implied that the water lines were super-Lorentzian (having a higher wing absorption than that predicted by the Lorentz or Voigt profiles). Since far wing deviations from the Lorentz or Voigt line shapes have been observed elsewhere for both CO₂ [12, 13] and H₂O [14], an adjustable line shape was employed. This shape is based on Lorentz or Voigt profile but allows for modification of the line wings using adjustable parameters.

The super-Lorentz profile employed was that developed by Trusty [15] which is similar in form to one previously proposed by Benedict [16]. The shape factors for this profile are:

$$f(\gamma, \nu - \nu_0) = \frac{C\gamma}{\pi[(\nu - \nu_0)^2 + \gamma^2]} \text{ for } |\nu - \nu_0| \leq \nu_m \quad (14)$$

$$f(\gamma, \nu - \nu_0) = \frac{C\gamma}{\pi(\nu_m^2 + \gamma^2)} \left(\frac{\nu_m}{\nu - \nu_0} \right)^\eta \text{ for } |\nu - \nu_0| \geq \nu_m \quad (15)$$

where the Lorentz shape is used near line center, $(\nu - \nu_0) \leq \nu_m$, and a modified shape is assumed in the wings $(\nu - \nu_0) > \nu_m$. In these equations both ν_m and η are empirically determined parameters while C is a normalization constant. If ν_m is taken as $G\gamma_L$ where G is some integer and γ_L the Lorentz half width, C is found to be

$$c = (\pi/2) / \left\{ \tan^{-1}(G) - \frac{G}{[G^2 + 1][1 - \eta]} \right\} \quad (16)$$

Since this profile is essentially a modification of the Lorentz or pressure broadened line shape, it should be applicable to higher pressures where collisional broadening is dominant. At intermediate or lower pressures such as those encountered in the upper atmosphere, Doppler broadening becomes increasingly significant and a combined line shape similar to the Voigt profile must be used. To insure proper treatment of this pressure regime a "super-Voigt" profile was derived by taking the convolution of the Doppler distribution with Eq. (15). The resulting convolution integral could not be solved directly so a series solution was derived which was valid for the far wings of a Lorentz line while numeric integration was used to evaluate this function in the near wings.*

The super-Voigt profile like the super-Lorentz still depends on the two empirical parameters ν_m and η . Because the super-Voigt shape is fairly insensitive to the value of ν_m [15], this parameter was taken as $3(\gamma_L)$ (the optimum value determined in reference 14), this being considered a reasonable bound for the validity of the pressure broadened line shape. At pressures and temperatures for which the absorption coefficient is dominated by far wings, Eq. (15) predicts the variation in the calculated absorption coefficient with η to be:

$$\frac{\delta K(\nu)}{K(\nu)} = \phi(P_e, T) \delta \eta . \quad (17)$$

*Details of the derivation of the super-Voigt profile are given in Appendix A.

Where T is the absolute temperature, P_e the effective pressure given by $(P_f + BP_s)$ as in Eq. (10), and

$$\phi(P_e, T) = \frac{\sum_i k_i(P_e, T) \ln [v_{m_i}(P_e, T) / (v - v_{o_i})]}{\sum_i k_i(P_e, T)}$$

k_i being the contribution to the total absorption coefficient by the i^{th} spectral line. Although ϕ depends on temperature in a very complex fashion, it may be shown that its pressure dependence is given by

$$\phi(P_e, T) = \phi(1, T) + \ln(P_e) \quad (18)$$

where, since ϕ is negative, the variation in $K(v)$ will decrease with increasing pressure. Calculated values of the absorption coefficients for all the laser lines in general followed both Eq. (17) and Eq. (18) for values of P_e below approximately 200 torr with larger values of ϕ being observed at higher temperatures as shown in Figure 23. Consequently, an iterative procedure was developed for evaluating η in which absorption coefficients were calculated for each laser line and the value of η varied using Eq. (17) until a "best-fit" value was found

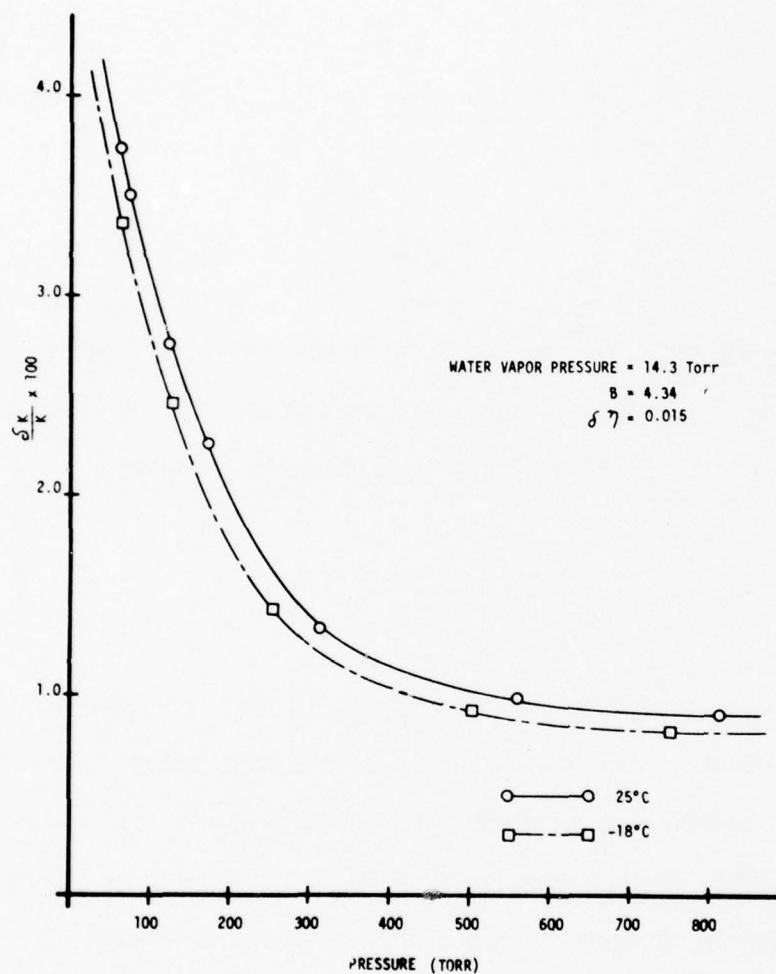


Figure 23. Observed pressure and temperature dependence of $\delta K/K$ for laser line $P_1(6)$.

for all laser lines.* In general this process was successful since a single η value could be found which substantially increased the predictions for those lines which were originally underpredicted while only slightly changing the calculated values for those already in near agreement. However, the calculated coefficient at laser line $P_1(7)$ was still significantly low; and an attempt to force agreement on this line pushed the values for all other lines above their measured values. A second iteration was therefore attempted using the original AFGL line parameters in the vicinity of $P_1(7)$.** In this case agreement within experimental error could be obtained for most lines using

$$\eta = 1.88.$$

In the case of lines $P_2(5)$ and $P_2(6)$ however, slight modifications to the self broadening parameter B were also required: the value at $P_2(5)$ being

*Absorption coefficients for laser line $P_1(4)$ were not considered in this fit process because of their strong dependence on HDO and other isotopic lines for which accurate strengths, positions, and widths were not known.

***An obvious line position error for water line $5_{4,1} \rightarrow 4_{1,4}$ $V = 0, 0, 0 \rightarrow 0, 2, 0$ was corrected in the AFGL tabulation using the observed position of Rao et al. in reference 17.

taken as 6.30 instead of 7.12, while the value at $P_2(6)$ was taken as 3.91 instead of 4.82. Comparisons of measured and calculated coefficients for all laser lines using this value of η and the modified line tabulations [except for $P_1(8)$ and $P_3(5)$] are presented in Appendix B. Data for lines $P_1(8)$ and $P_3(5)$ were obtained for only two cell conditions: 14.3 torr of water at 25°C buffered with air to 75.0 torr and 764.3 torr. For these conditions the measured absorption coefficients for $P_1(8)$ were 27.10 and 131.3 km^{-1} , respectively, while those for $P_3(5)$ were 0.680 and 3.358 km^{-1} . Although super-Voigt calculations were not done for these lines, standard Voigt predictions agreed well with the observed values for $P_1(8)$ and were lower for $P_3(5)$. Further analysis on these lines was not attempted.

Although the super-Voigt shape did not bring the calculations into perfect agreement for all HF laser lines, it did substantially improve the predictions in most cases. Thus the calculations presented here do give credence to super-Lorentz or super-Voigt behavior in water vapor, since the changes in the calculated absorption coefficients with the super-Voigt shape are of the right magnitude for the various laser lines: large increases being obtained at those frequencies for which the pure Lorentz values were substantially low and only slight increases being obtained where the Lorentz predictions were in near agreement.

In addition to the measurements of air (O_2/N_2) broadened H_2O absorption coefficients, limited data were also collected for oxygen broadened H_2O absorption as well as air broadened CO_2 absorption. The oxygen broadened water vapor data were collected at HF laser lines $P_1(4)$, $P_1(6)$, $P_1(7)$, $P_2(5)$, and $P_2(6)$ using a water vapor partial pressure of 14.3 torr and an oxygen buffer pressure of 60.7 torr. Oxygen is known to be a less effective foreign-gas-broadener for water vapor than nitrogen having an average ratio of $\gamma_{O_2}/\gamma_{air}$ of 0.5236 [18]. Consequently, calculations were performed at the above laser line frequencies using an effective buffer pressure of 31.8 torr or $(0.5236) \times (60.7)$ torr. The results of these calculations using the modified AFGL tabulation with both the Voigt and super-Voigt profiles are given in Table 4. It may be seen from this data that again the super-Voigt profile gives substantially better agreement than the standard Voigt profile implying that the water lines are super-Lorentzian even when oxygen broadened. The discrepancy observed for line $P_1(4)$, as seen before in the air broadened data, is due to the strong isotopic water vapor absorption near this laser line for which accurate strengths, positions, and widths are not known.

Strong CO_2 absorption was observed for HF laser lines $P_1(6)$, $P_1(7)$ and $P_2(5)$. Measurements for these lines were made with air broadening (80/20 mixture of N_2/O_2) using a CO_2 partial pressure of 0.434 torr buffered to total pressures of 760 and 75 torr and a CO_2 pressure of 3 torr buffered to 75 torr. Results of these measurements are given in

TABLE 4
OBSERVED AND CALCULATED ABSORPTION COEFFICIENTS FOR SELECTED
HF LASER LINES WITH OXYGEN BROADENING

$$\gamma_{O_2}/\gamma_{air} = 0.5236$$

$$P_{H_2O} = 14.3 \text{ TORR}, P_{O_2} = 60.7 \text{ TORR}, T = 25^\circ\text{C}$$

ABSORPTION COEFFICIENTS (km^{-1})			
<u>Laser Line</u>	<u>Voigt Profile</u>	<u>Observed</u>	<u>Super-Voigt Profile</u>
P ₁ (4)	2.426	5.910	3.463
P ₁ (6)	29.380	39.10	33.95
P ₁ (7)	8.816	12.11	11.57
P ₂ (5)	9.487	11.25	11.22
P ₂ (6)	6.985	8.690	8.264

Table 5 and are compared to calculated values based on the AFGL tape using the Voigt profile. It may be seen that the calculated values for lines $P_1(6)$ and $P_2(5)$ are within the experimental uncertainty while those for laser line $P_1(7)$ are consistently high. Although a thorough investigation of these errors was outside the scope of present work, the line strengths in the vicinity of line $P_1(7)$ were checked using the work of Gray et al. [19] and no significant errors were found. Because several experimental studies have indicated that CO_2 lines are definitely sub-Lorentzian [12, 13] it may be that the overprediction for laser line $P_1(7)$ is a line shape problem and not a deficiency in the tabulated line parameters. Further investigation of this behavior is required.

DISCUSSION

Calculation of absorption coefficients at HF laser frequencies using line-by-line calculations based on the AFGL tabulation were found to be improved by modifying the tabulation using the line positions and strengths of reference 8 and by introducing a super-Lorentz or super-Voigt line shape. The present study is by no means exhaustive, however, and several questions remain:

1. The line positions, strengths, and widths for isotopic water species in this spectral region appear to be in error as demonstrated by the discrepancies observed for laser line $P_1(4)$.

TABLE 5
OBSERVED AND CALCULATED ABSORPTION COEFFICIENTS FOR CARBON DIOXIDE

$P_{\text{total}} = 760 \text{ TORR}, P_{\text{CO}_2} = 0.434 \text{ TORR}$

<u>Laser Line</u>	<u>Frequency (cm^{-1})</u>	<u>Observed (km^{-1})</u>	<u>Calculated (km^{-1})</u>
$P_1(6)$	3693.4226	5.44	5.07
$P_1(7)$	3644.1454	7.30	8.52
$P_2(5)$	3577.5002	9.85	9.32

$P_{\text{total}} = 75 \text{ TORR}, P_{\text{CO}_2} = 0.434 \text{ TORR}$

<u>Laser Line</u>	<u>Frequency (cm^{-1})</u>	<u>Observed (km^{-1})</u>	<u>Calculated (km^{-1})</u>
$P_1(6)$	3693.4226	0.570	0.632
$P_1(7)$	3644.1454	1.12	1.58
$P_2(5)$	3577.5002	2.63	2.94

$P_{\text{total}} = 75 \text{ TORR}, P_{\text{CO}_2} = 3.0 \text{ TORR}$

<u>Laser Line</u>	<u>Frequency (cm^{-1})</u>	<u>Observed (km^{-1})</u>	<u>Calculated (km^{-1})</u>
$P_1(6)$	3693.4226	4.56	4.40
$P_1(7)$	3644.1454	7.39	11.07
$P_2(5)$	3577.5002	18.1	20.4

2. The assumption of super-Lorentz behavior for water vapor appears to be supported by the present data but lacks direct experimental verification through observation of far wing absorption of individual H_2O lines. Many of the same effects observed with the super-Lorentz shape could be duplicated by modification of line strengths, widths, and positions in the AFGL tabulation.

3. The super-Lorentz profile assumed here is strictly an empirical modification of the Lorentz shape and needs theoretical support. Since in fitting experimental data for CO_2 [12, 13] a sub-Lorentz shape was found to be necessary in which the line wings became sub-Lorentzian in an exponential fashion, the assumed form of the present super-Lorentz shape may not be ideal.

4. The self-to-foreign broadening ratios (B) determined here are based on minimal data at a single temperature. Further verification of these values is required as well as a study of any possible temperature dependencies. Since in general these ratios will vary from one spectral line to another, ideally values should be evaluated for all absorption lines of interest instead of measuring effective average values.

5. Substantial scatter was observed in the measured absorption coefficients below 0.1 km^{-1} . Since most low temperature data was in this

range, further low temperature measurements are required to check the calculational methods before applying them to high altitude low temperature problems.

CALCULATED ABSORPTION COEFFICIENTS FOR MODEL ATMOSPHERES

Total absorption coefficients for HF laser lines $P_1(4)$, $P_1(6)$, $P_1(7)$, $P_2(5)$, $P_2(6)$, $P_2(7)$, and $P_2(8)$ have been calculated as a function of altitude and relative humidity using atmospheric temperature and pressure profiles, corresponding to the midlatitude summer model [20], shown in Table 6.* The concentrations assumed for the evenly mixed atmospheric constituents (those invariant with altitude) are given in Table 7. In performing these calculations the modified line tabulations and the super-Voigt profile, discussed above, were used for water vapor while the AFGL tabulation and standard Voigt profile were used for the other atmospheric constituents.

The results of these calculations are shown in Figures 24 through 30 for relative humidities of 10, 30, 50, 70, and 90% covering altitudes

**Since there is no significant ozone absorption in this spectral region the ozone concentration has been taken as zero in these calculations.*

TABLE 6
ATMOSPHERIC CONDITIONS USED IN CALCULATING ABSORPTION COEFFICIENTS
AS A FUNCTION OF ALTITUDE FOR HF LASER LINES

Altitude (km)	Temperature (K)	Total Pressure (torr)	Saturated H ₂ O Pressure (torr)
0	294	760.00	18.65
1	290	676.72	14.53
2	285	601.70	10.52
3	279	532.67	7.013
4	273	471.15	4.579
5	267	415.64	2.765
6	261	365.37	1.632
7	255	319.60	0.9390
8	248	279.09	0.4760
9	242	243.08	0.2590
10	235	210.82	0.1210
11	229	182.31	0.0609
12	222	156.80	0.0263
13	216	134.29	0.0122
14	216	114.79	0.0122
15	216	97.53	0.0122

HDO concentration = 0.03% of H₂O concentration

TABLE 7
ASSUMED CONCENTRATIONS OF EVENLY MIXED
ATMOSPHERIC CONSTITUENTS

Species	Concentration PPM by Volume
CO ₂	330
N ₂ O	0.28
CO	0.075
CH ₄	1.60
O ₂	2.095 x 10 ⁵

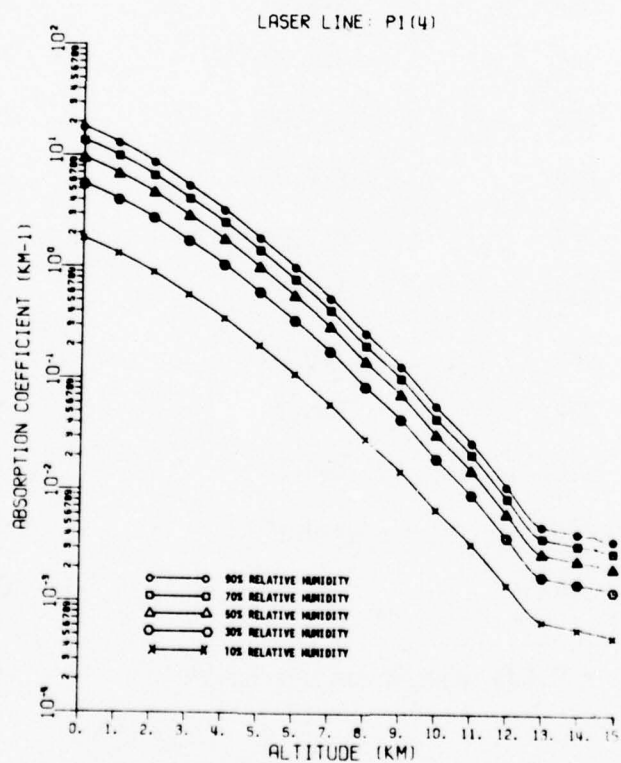


Figure 24. Absorption coefficients as a function of altitude and relative humidity for laser line P₁(4).

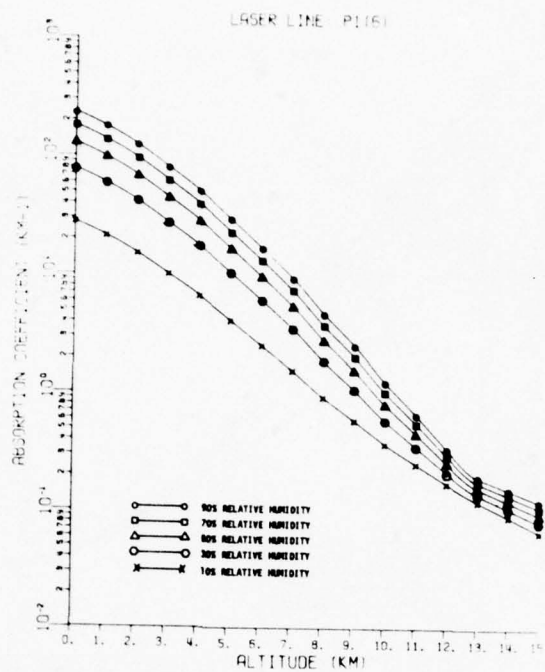


Figure 25. Absorption coefficients as a function of altitude and relative humidity for laser line P₁(6).

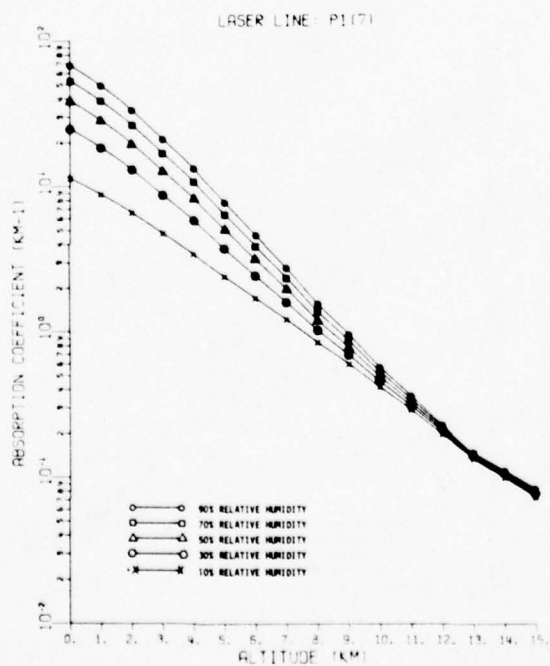


Figure 26. Absorption coefficients as a function of altitude and relative humidity for laser line P₁(7).

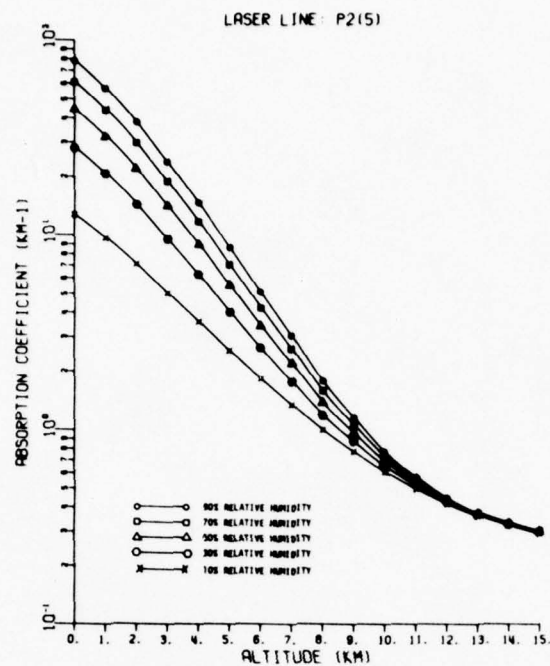


Figure 27. Absorption coefficients as a function of altitude and relative humidity for laser line P₂(5).

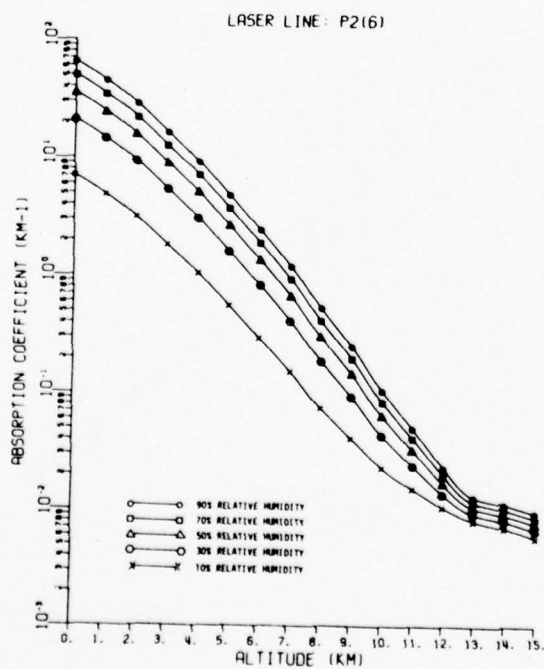


Figure 28. Absorption coefficients as a function of altitude and relative humidity for laser line P₂(6).

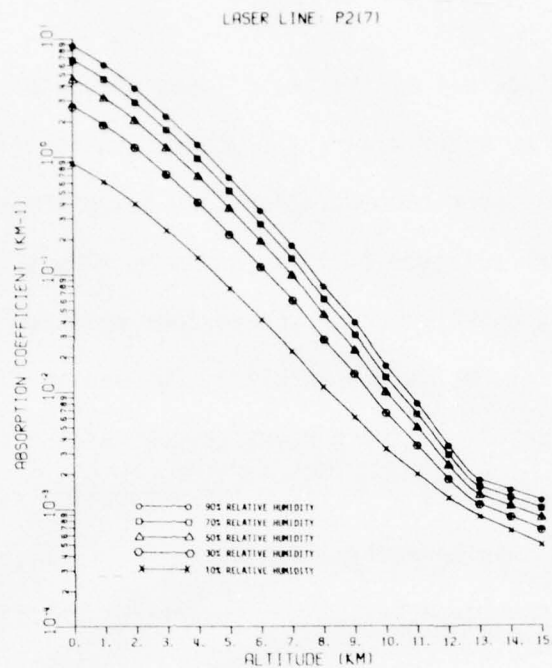


Figure 29. Absorption coefficients as a function of altitude and relative humidity for laser line P₂(7).

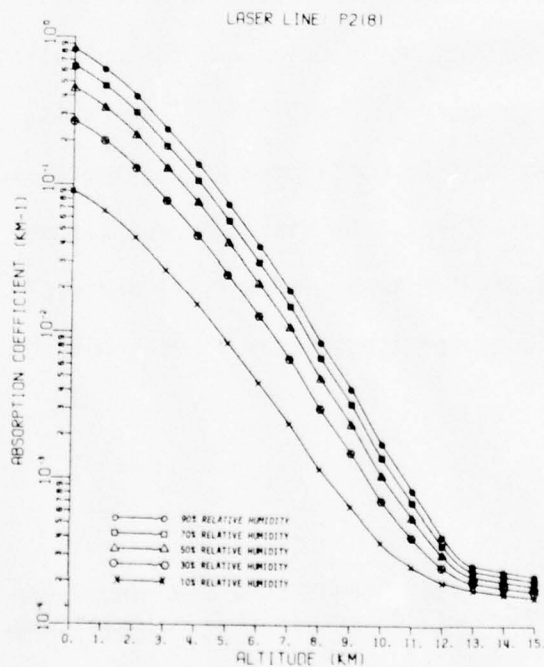


Figure 30. Absorption coefficients as a function of altitude and relative humidity for laser line P₂(8).

from 0 to 15 km. Since all of the laser lines presented here are strongly attenuated by water vapor, the absorption coefficients vary roughly as the water vapor concentration (and hence temperature) decreases rapidly to an altitude of 13 km and more slowly above this point. The observed convergence of the various relative humidity curves at higher altitudes is the result of CO_2 and to a lesser extent N_2O absorptions since the percent concentrations of these species are invariant with altitude. In effect the absorption coefficients for laser lines showing this behavior, such as $P_1(6)$, $P_1(7)$, and $P_2(5)$, simply converge to the combined CO_2 - N_2O absorption coefficient at higher altitudes.

Although calculations were carried to an altitude of 15 km, the experimental data gathered in the present study did not cover temperatures below -18°C (255K) so that verification of the calculational methods for conditions above 7 km was not possible.* As a result, calculations for altitudes above 7 km must be considered as extrapolations based on higher temperature data. Similarly, the discrepancies between measured and calculated coefficients for laser lines $P_1(4)$ and $P_2(7)$ indicate that the calculated coefficients for these laser lines should be used with caution.

**Data being gathered at the present time covering lower temperatures will allow verification of higher altitude calculations.*

CONCLUSION

During the course of this parametric temperature and pressure study of the absorption of HF laser radiation by water vapor, a more accurate data base for atmospheric gaseous absorption coefficients was compiled. Several important characteristics of the absorption were investigated leading to changes in the method of predictive modeling of water vapor absorption which will better meet Army and Air Force requirements in the 3-5 μ m spectral region. Also pertinent parameters were defined which require further investigation before accurate predictions of atmospheric gaseous absorption above 7 km altitude can be made.

Only by the use of line-by-line modeling can sufficient resolution be obtained to calculate the absorption coefficients for the discrete HF laser frequencies. The self broadening coefficient B is an important parameter in such calculations especially at low buffer pressures. There is a different self broadening coefficient associated with each absorption line resulting in a complex dependence of B on pressure, temperature and frequency. An average self broadening coefficient of necessity is used because an exact value at each desired frequency for every atmospheric condition of interest would be prohibitively costly to calculate. In the HF spectral region the average B value commonly used is 5.0 which is in good agreement with the values obtained in this work and listed in Table 3 for 25°C. Variations in this parameter from

laser line to laser line are indicative of the complex functional dependence. Further investigation is needed to better define the self broadening coefficient dependence on temperature which may strongly affect water vapor absorption above 7 km altitude.

Just as important to accurate predictive model calculations is the absorption line data base - the best available one being the AFGL line parameter compilation. The present work indicates that some updating is needed. The Flaud and Camey Peyret $^1\text{H}_2$ ^{16}O line strengths and positions gave significantly improved predictions when compared with the presently used tape values. Discrepancies between updated model predictions for $P_1(4)$ and $P_2(7)$ indicate additional updating is needed especially in the HDO line parameters which may become increasingly important to accurate predictions above 7 km for laser lines lying near isotopic absorptions.

The most general result of this water vapor absorption study having impact on the 3-5 μm spectral region is the development of a super-Voigt line shape and computational capability. Significantly improved agreement between model calculations and measured absorption coefficients for HF lines dominated by far wing absorption is obtained with this model, and its influence on water vapor absorption will be enhanced at altitudes above 7 km. Here again a temperature dependence of the line shape may be significant and requires further investigation.

The worth of this parametric temperature and pressure measurement study is seen by comparing the measurements to the theoretical calculations before and after the above line parameter changes were included. Substantial agreement now exists between the calculations and measurements as seen in Appendix B except for lines $P_1(4)$ and $P_2(7)$ which still have unacceptable calculated absorption coefficients for accurate modeling purposes. Extrapolation of the present parametric study of water vapor absorption gives better estimates for the absorption coefficients above 7 km altitude as detailed in Figures 24 through 30. Accurate slant path modeling to or at such altitudes will require additional research. Between 12 and 18 km altitude, the dominance of the water vapor absorption is rivaled by CO_2 and N_2O whose concentrations do not fall off as quickly as water vapor with decreasing temperature and pressure. Some insight to the problem is seen in the narrowing of the separation of the five relative humidity curves in Figures 24 through 30 for altitudes above 12 km. The degree of agreement in this work at 25°C for CO_2 absorption at $P_1(6)$, $P_1(7)$ and $P_2(5)$ is not sufficient for high altitude predictions. The question of a sub-Lorentzian (or Voigt) line shape for CO_2 absorption needs investigation. Addressing these problem areas will yield the necessary data base to accurately model slant path gaseous absorption through the atmosphere and will be the subject of Part II.

APPENDIX A

METHODS OF EVALUATION FOR THE SUPER-VOIGT LINE PROFILE

The super-Voigt profile like the standard Voigt is defined as the convolution of the super-Lorentz and Doppler line shapes. Since the Doppler shape factor is given by

$$f_D(v, v') = \beta \exp [-(\ln 2)(v - v')^2 / \gamma_D^2] \quad (\text{A-1})$$

where β is a normalization constant, and the super-Lorentz shape is

$$f_{s1}(v, v_0) = \frac{C\gamma_L}{\pi[(v - v_0)^2 + \gamma_L^2]}, \quad \text{for } |(v - v_0)| < v_m; \quad (\text{A-2})$$

$$f_{s2}(v, v_0) = \frac{C\gamma_L(v_m)^n}{\pi(v_m^2 + \gamma_L^2)} \left(\frac{1}{v - v_0} \right)^n, \quad \text{for } |(v - v_0)| \geq v_m. \quad (\text{A-3})$$

The convolution integral for the super-Voigt absorption coefficient is expressed as:

$$\begin{aligned} K_V(v') = S \int_{-\infty}^{a-v_m} f_D(v, v') f_{s2}(v, v_0) d(v - v') \\ + S \int_{a-v_m}^{a+v_m} f_D(v, v') f_{s1}(v, v_0) d(v - v') \end{aligned}$$

$$+ S \int_{a+v_m}^{\infty} f_D(v, v') f_{s2}(v, v_0) d(v - v') \quad (A-4)$$

where S is the line strength and $a = (v_0 - v')$, the separation of the point of computation from the center of the Lorentz line. Because of the exponential fall-off of the Doppler profile, in most cases of interest only one or two of these integrals will make a significant contribution. If for example

$$v_m < |a| < v_m + 6\gamma_D$$

as shown in Figure A-1, then both the second and third integrals of Eq. (A-4) will be significant; while if

$$|a| \geq v_m + 6\gamma_D \quad (A-5)$$

as in Figure A-2 only the third integral will contribute.* In general the integrals of Eq. (A-4) may not be solved directly so that numerical integration procedures are required. An exception to this is that when Eq. (A-5) is satisfied, a series solution may be found for the one contributing integral. This solution is significant since in normal atmospheric transmission calculations the majority of the lines contributing to the absorption at a given frequency are far enough removed from this frequency so that Eq. (A-5) is satisfied. Consequently, a reasonable fraction of the computational time (and hence cost) may be saved by using a series solution

* $(v - v') = 6\gamma_D$ has been taken as a reasonable bound beyond which the Doppler profile will be so small that the convolution integral may be terminated.

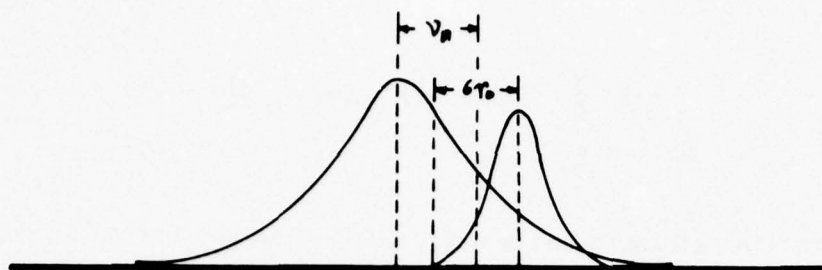


Figure A-1. Schematic of the convolution of Doppler and Lorentz line shapes for

$$\nu_m < |a| < \nu_m + 6\gamma_D$$

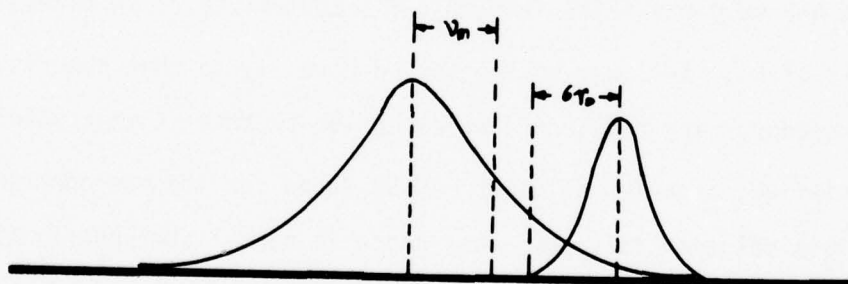


Figure A-2. Schematic of the convolution of Doppler and Lorentz line shapes for

$$|a| \geq \nu_m + 6\gamma_D$$

for these lines instead of having to resort to numerical integration techniques.

Considering first the case where Eq. (A-5) is satisfied, the absorption coefficient of Eq. (A-4) reduces to:

$$K_V(\nu') = \frac{CS \gamma_L \nu_m^\eta}{\pi(\nu_m^2 + \gamma_L^2)} \beta \int \frac{\exp [-(\ln 2)(\nu - \nu')^2 / \gamma_D^2]}{(\nu_0 - \nu)^\eta} d(\nu - \nu') \quad (A-6)$$

This may be put in a more standard form by substituting

$$w = \sqrt{\ln 2} [(\nu - \nu') / \gamma_D]$$

and

$$\xi = \sqrt{\ln 2} [(\nu_0 - \nu') / \gamma_D] \quad (A-7)$$

giving:

$$K_V(\nu') = \frac{CS \gamma_L \nu_m^\eta \beta}{\pi(\nu_m^2 + \gamma_L^2)} \left(\frac{\sqrt{\ln 2}}{\gamma_D} \right)^{\eta-1} \int \frac{e^{-y^2} dw}{(\xi - w)^\eta} \quad (A-8)$$

Since the integral in this equation will not be taken over an infinite range the normalization constant β will be carried through the computations explicitly as

$$\beta = 1 / \int \exp [-(\ln 2)(v - v')^2 / \gamma_D^2] d(v - v') .$$

Using the same substitutions as before this becomes

$$\beta = \left(\sqrt{\ln 2} / \gamma_D \right) / \int e^{-w^2} dw$$

so that Eq. (A-8) may be written:

$$K_V(v') = \frac{CS \gamma_L}{\pi(\gamma_m^2 + \gamma_L^2)} \left(\frac{v_m \sqrt{\ln 2}}{\gamma_D} \right)^\eta \int \frac{e^{-w^2} dw}{(\xi - w)^\eta} / \int e^{-w^2} dw . \quad (A-9)$$

Since Eq. (A-5) is satisfied it also follows that

$$w/\xi < 1$$

so that

$$\begin{aligned} \frac{1}{(\xi - w)} &= \frac{1}{\xi^\eta} (1 - w/\xi)^{-\eta} \\ &= \frac{1}{\xi^\eta} \left\{ 1 + \sum_{i=1}^{\infty} \frac{n(n+1)(n+2)\dots(n+i-1)}{i!} (w/\xi)^i \right\} . \end{aligned}$$

Substituting this into Eq. (A-9) gives

$$K_V(\nu') = K_S(\nu') \left\{ 1 + \sum_{i=1}^{\infty} \frac{N(i)}{\xi^i} \left[\int e^{-w^2} w^i dw / \int e^{-w^2} dw \right] \right\} \quad (A-10)$$

where $K_S(\nu')$ is the super-Lorentz absorption coefficient given by Eq. (A-3) times the line strength (S), while $N(i)$ has been defined as

$$N(i) = \frac{\eta(\eta+1)(\eta+2)\dots(\eta+i-1)}{i!} . \quad (A-11)$$

If the integrals in Eq. (A-10) are taken over some even range say from $-\alpha$ to $+\alpha$ only even powers of w^i will have nonvanishing contributions. Consequently, Eq. (A-10) may be rewritten as:

$$K_V(\nu') = K_S(\nu') \left\{ 1 + \sum_{j=1}^{\infty} \frac{N_j}{\xi^{2j}} I(j)/I(0) \right\} \quad (A-12)$$

where:

$$N_j = \frac{\eta(\eta+1)(\eta+2)\dots(\eta+2j-1)}{(2j)!} \quad (A-13)$$

and

$$I(j) = \int_{-\alpha}^{\alpha} w^{2j} e^{-w^2} dw . \quad (A-14)$$

Integration of Eq. (A-14) by parts gives a recurrence relation for the $I(j)$'s such that:

$$I(j) = -\alpha^{2j-1} e^{-\alpha^2} + \frac{(2j-1)}{2} I(j-1) \quad (A-15)$$

with

$$I(0) = \int_{-\alpha}^{\alpha} e^{-w^2} dw. \quad (A-16)$$

If α is then taken as 5 so that the integration is carried out to $(v - v')$ $\approx 6\gamma_D$, numeric integration shows that the value of $I(0)$ is essentially the same as that for $\alpha \rightarrow \infty$ or

$$I(0) = \sqrt{\pi}. \quad (A-17)$$

Eqs. (A-12), (A-13), (A-15), and (A-17) then define the series solution to the convolution integral of Eq. (A-9). These equations may be put in a more convenient form as:

$$K_V(v') = K_S(v') \left\{ 1 + \sum_{j=1}^{\infty} A(j) [I(j)/I(0)] \right\} \quad (A-18)$$

$$A(j) = A(j-1) [\eta + 2(j-1)] [\eta + 2j - 1] / (2j)(2j-1)\xi^2 \quad (A-19)$$

$$I(j) = -\alpha^{2j-1} e^{-\alpha^2} + \frac{(2j-1)}{2} I(j-1) \quad (A-20)$$

where

$$I(0) = \sqrt{\pi} \text{ and } A(1) = \frac{\eta(\eta+1)}{2\xi^2} \quad (A-21)$$

and

$$K_S(\nu') = \frac{CS \gamma_L}{\pi(\nu_m^2 + \gamma_L^2)} \left(\frac{\nu_m}{\nu' - \nu_o} \right)^\eta. \quad (A-22)$$

A further simplification is possible if $\xi \geq 5$ and

$$1.0 \leq \eta \leq 2.0.$$

Under these conditions the series converges to the numerically integrated value of Eq. (A-9) to within one part in 10^6 using a maximum of 10 terms. By considering the relative magnitudes of these terms it is found that the first term of Eq. (A-20)

$$- \alpha^{2j-1} e^{-\alpha^2}$$

may be ignored relative to the second term

$$\frac{(2j-1)}{2} I(j-1)$$

so that the absorption coefficient may be evaluated using:

$$K_V(\nu') = K_S(\nu') \left\{ 1 + \sum_{j=1}^N H(j) \right\} \quad (A-23)$$

where $K_S(\nu')$ is the same as that of Eq. (A-22) and

$$H(j) = H(j-1) \frac{[\eta + 2(j-1)](\eta + 2j - 1)}{4j \xi^2} \quad (A-24)$$

with

$$H(1) = \frac{n(n+1)}{4\xi^2} . \quad (A-25)$$

From Eqs. (A-9) and (A-18) it follows that

$$\int \frac{e^{-w^2} dw}{(\xi - w)^\eta} \bigg/ \int e^{-w^2} dw = \frac{1}{\xi^\eta} \left\{ 1 + \sum_{j=1}^N H(j) \right\} . \quad (A-26)$$

Consequently, the approximate series solution of Eqs. (A-23) through (A-25) was checked by testing the equality of this equation when the left hand side was evaluated using numerical integration techniques. For ξ greater than 5 and η between 1.0 and 2.0 the series solution gave the same result as the numerical integration to within one part in 10^7 using up to 11 terms in the series. Therefore, Eqs. (A-23) through (A-25) were used exclusively in the computer code to evaluate the super-Voigt absorption coefficient for all lines satisfying the condition

$$(\nu_0 - \nu') \geq \nu_m + 6\gamma_D . \quad (A-27)$$

The summation in the computer program was carried through as many terms as required in order for the next term to be less than 10^{-6} of the running sum. Generally this took less than 10 terms.

If spectral lines contributed to the total absorption coefficient which did not satisfy the inequality of Eq. (A-27), the integrals of Eq. (A-4)

were evaluated using Trapezoidal integration with sixteen intervals being used between $w = +5$ and $w = -5$. The exception to this was when spectral lines fell within v_m of the frequency at which the coefficient was being evaluated, that is when

$$(v_o - v') < v_m .$$

Under these circumstances the contribution to the total absorption coefficient from these lines was evaluated with the normal Voigt profile using the procedures defined in reference 15.

APPENDIX B
MEASURED AND CALCULATED ABSORPTION COEFFICIENTS
FOR SELECTED HF LASER LINES

This appendix presents all of the measured absorption coefficients in Table B-1 for HF laser lines: $P_1(4)$, $P_1(6)$, $P_1(7)$, $P_2(5)$, $P_2(6)$, $P_2(7)$, and $P_2(8)$ covering the experimental conditions outlined in Table 1 (page 22). In addition, two sets of calculated coefficients are also presented which have been obtained using:

1. The AFGL tabulation in conjunction with the standard Voigt line profile.
2. The modified line tabulations and super-Voigt profile discussed in the text.

Comparison of the calculated and measured values indicates the improvement in the predictability of the coefficients using the modified tabulations and line shape.

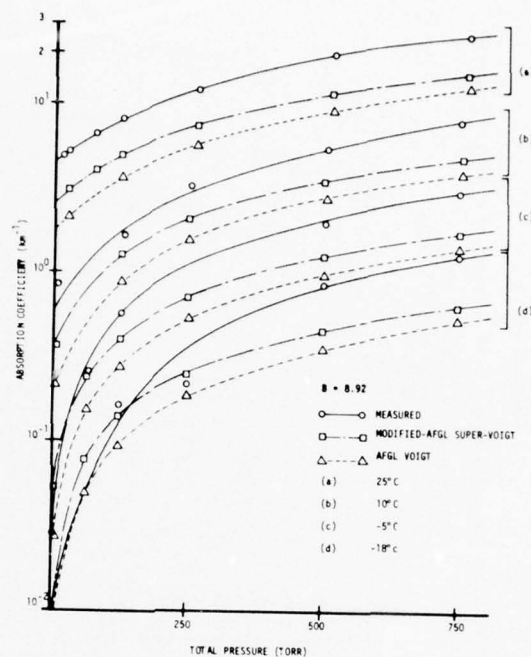


Figure B-1. Measured and calculated absorption coefficients for laser line $P_1(4)$.

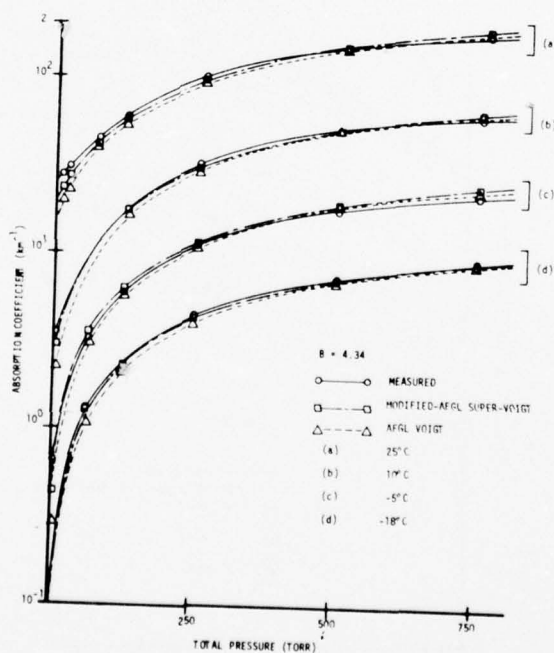


Figure B-2. Measured and calculated absorption coefficients for laser line $P_1(6)$.

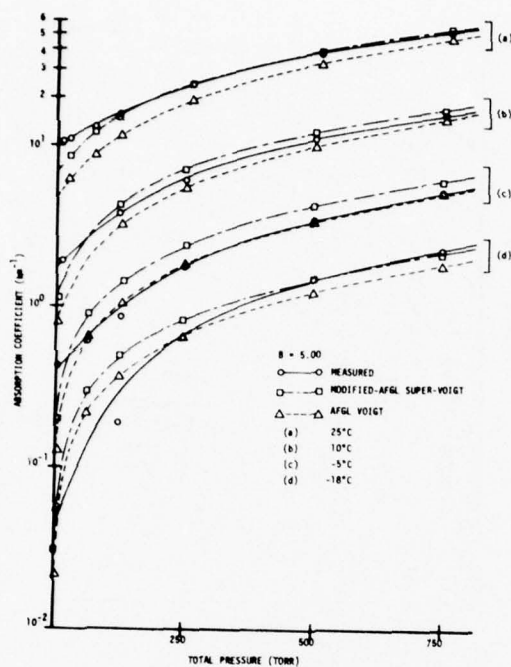


Figure B-3. Measured and calculated absorption coefficients for laser line $P_1(7)$.

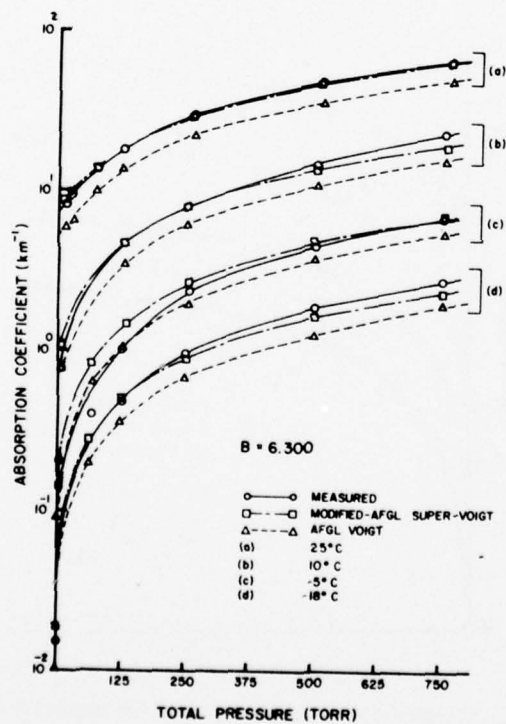


Figure B-4. Measured and calculated absorption coefficients for laser line $P_2(5)$.

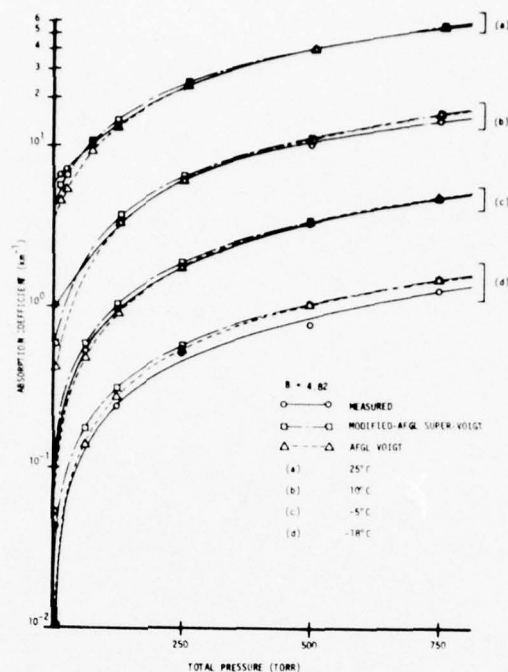


Figure B-5. Measured and calculated absorption coefficients for laser line $P_2(6)$.

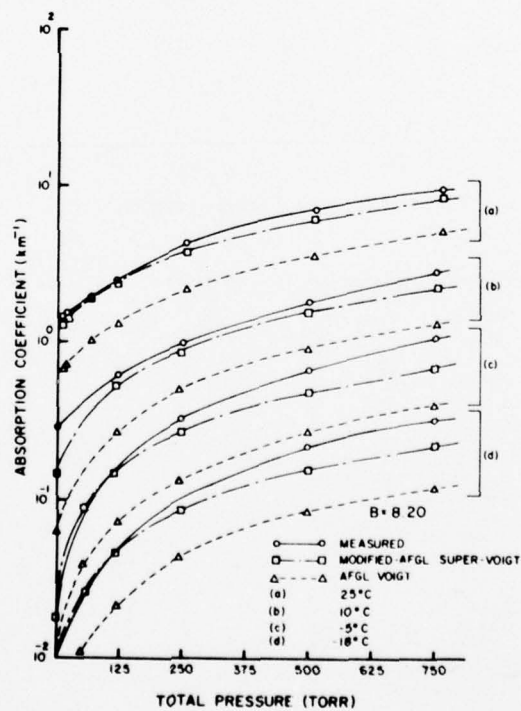


Figure B-6. Measured and calculated absorption coefficients for laser line $P_2(7)$.

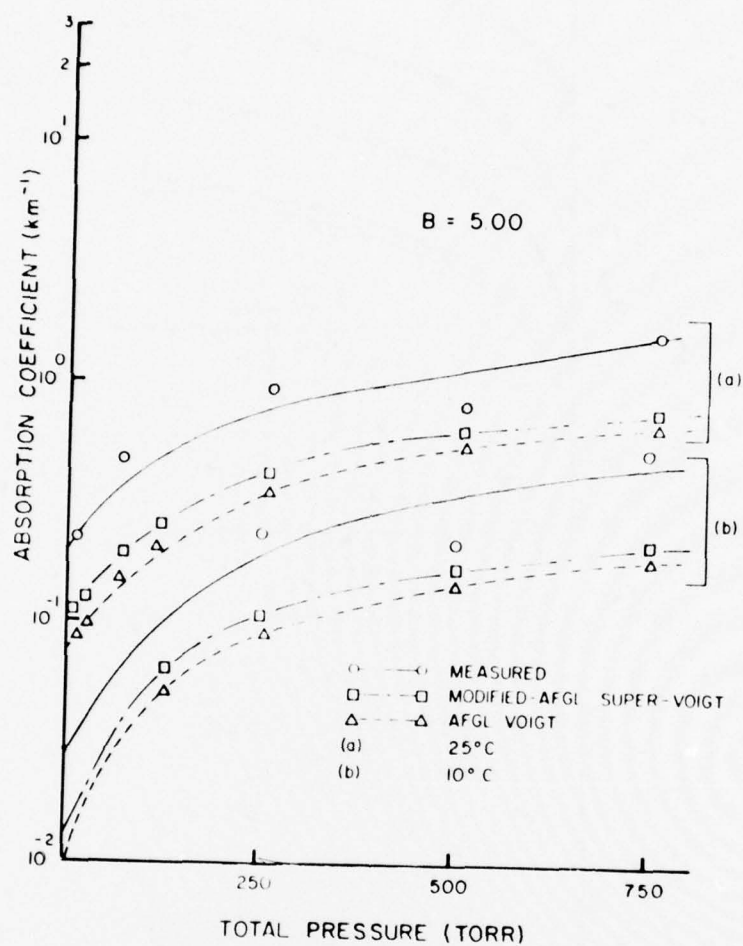


Figure B-7. Measured and calculated absorption coefficients for laser line P(8).

TABLE B-1
WATER VAPOR ABSORPTION COEFFICIENTS FOR SELECTED HF LASER LINES

Temperature (°C)	25	25	25	10	-5	-18
Water Vapor Pressure (Torr)	14.30	10.00	5.00	4.50	1.50	0.50
$P_1(4)$	4.885	2.673	0.900	0.620	0.028	0.001
Table Entries:	0.000	15.00	20.00	0.000	0.000	0.000
Upper Entry	5.203	3.620	1.440	1.750	0.290	0.150
absorption	10.70	65.00	70.00	125.0	62.50	125.0
coefficient*	6.598	4.715	2.006	2.950	0.570	0.218
(km^{-1})	60.70	115.0	120.0	250.0	125.0	250.0
Lower Entry	8.128			5.433	1.120	0.873
air buffer	110.7			500.0	250.0	500.0
pressure (torr)	12.05			7.864	2.120	1.301
	250.0			750.0	500.0	750.0
	19.72				3.015	
	500.0				750.0	
	25.53					
	750.0					

*The precision of the absorption coefficients is four significant digits truncated for small values below 10^{-3} . The accuracy of the measurements is typically 0.01 km^{-1} or 10%, whichever is greater.

Table B-1 (cont)

$P_1(6)$	28.39	17.03	5.934	3.529	0.422	0.050
<u>Table Entries:</u>	0.000	15.00	20.00	0.000	0.000	0.000
<u>Upper Entry</u>	30.09	29.01	11.91	17.99	3.248	1.304
<u>absorption</u>	10.70	65.00	70.00	125.0	62.50	62.50
<u>coefficient</u>	44.99	39.69	17.51	32.53	5.980	2.245
<u>(km⁻¹)</u>	60.70	115.0	120.0	250.0	125.0	125.0
<u>Lower Entry</u>	60.76			51.11	10.97	4.415
<u>air buffer</u>	110.7			500.0	250.0	250.0
<u>pressure (torr)</u>	102.5			61.44	17.93	7.149
	250.0			750.0	500.0	500.0
	150.3				21.95	8.985
	500.0				750.0	750.0
	179.1					
	750.0					

$P_1(7)$	10.70	6.046	2.211	1.932	0.400	0.043
<u>Table Entries:</u>	0.000	15.00	20.00	0.000	0.000	0.000
<u>Upper Entry</u>	11.136	7.844	3.062	3.769	0.614	0.223
<u>absorption</u>	10.70	65.00	70.00	125.0	62.50	125.0
<u>coefficient</u>	12.88	9.846	3.954	5.938	0.320	0.590
<u>(km⁻¹)</u>	60.70	115.0	120.0	250.0	125.0	250.0
<u>Lower Entry</u>	15.74			10.77	1.770	1.484
<u>air buffer</u>	110.7			500.0	250.0	500.0
<u>pressure (torr)</u>						

Table B-1 (cont)

$P_1(7)$	23.86			15.22	3.337	2.203
Table Entries:	250.0			750.0	500.0	750.0
Upper Entry absorption coefficient (km^{-1})	37.25				5.002	
	500.0				750.0	
Lower Entry air buffer pressure (torr)	50.45					
	750.0					

$P_1(8)$	27.10					
Table Entries:	60.70					
Upper Entry absorption coefficient (km^{-1})	131.3					
	750.0					
Lower Entry air buffer pressure (torr)						

$P_2(5)$	8.469	4.905	1.587	0.799	0.100	0.015
Table Entries:	0.000	15.00	20.00	0.000	0.000	0.000
Upper Entry absorption coefficient (km^{-1})	9.164	8.017	3.210	4.606	0.455	0.449
	10.70	65.00	70.00	125.0	62.50	125.0
	13.42	10.85	4.600	7.796	1.025	0.950
Lower Entry air buffer pressure (torr)	60.70	115.0	120.0	250.0	125.0	250.0
	17.72			14.57	2.381	1.826
	110.7			500.0	250.0	500.0

Table B-1 (cont)

$P_2(5)$	29.51			22.99	4.470	2.720
Table Entries:	250.0			750.0	500.0	750.0
Upper Entry absorption coefficient (km^{-1})	47.67				6.737	
	500.0				750.0	
Lower Entry air buffer pressure (torr)	64.01					
	750.00					

$P_2(6)$	6.515	3.937	1.373	1.021	0.115	0.010
Table Entries:	0.000	15.00	20.00	0.000	0.000	0.000
Upper Entry absorption coefficient (km^{-1})	7.092	6.304	2.776	3.343	0.548	0.240
	10.70	65.00	70.00	125.0	62.50	125.0
Lower Entry air buffer pressure (torr)	10.46	8.742	3.925	6.103	0.972	0.535
	60.70	115.0	120.0	250.0	125.0	250.0
	13.54			10.34	1.747	0.840
	110.7			500.0	250.0	500.0
	23.83			14.79	3.352	1.170
	250.0			750.0	500.0	750.0
	40.97				4.653	
	500.0				750.0	
	54.94					
	750.0					

Table B-1 (cont)

$P_2(7)$	1.350	0.527	0.312	0.275	0.029	0.000
	0.000	15.00	20.00	0.000	0.000	0.000
<u>Table Entries:</u>	1.420	0.875	0.518	0.605	0.073	0.044
<u>Upper Entry</u> absorption coefficient (km^{-1})	10.70	65.00	70.00	125.0	62.50	125.0
<u>Lower Entry</u> air buffer pressure (torr)	1.850	1.384	0.634	0.901	0.145	0.100
	60.70	115.0	120.0	250.0	125.0	250.0
	2.394			1.695	0.325	0.210
	110.7			500.0	250.0	500.0
	4.099			2.621	0.640	0.320
	250.0			750.0	500.0	750.0
	6.619				1.016	
	500.0				750.0	
	8.557					
	750.0					

$P_2(8)$	0.219			0.025	0.080	
	0.000			0.000	0.000	
<u>Table Entries:</u>	0.240			0.100	0.170	
<u>Upper Entry</u> absorption coefficient (km^{-1})	10.70			125.0	125.0	
<u>Lower Entry</u> air buffer pressure (torr)	0.370			0.185	0.004	
	60.70			250.0	250.0	
	0.480			0.330	0.215	
	110.7			500.0	500.0	

Table B-1 (cont)

$P_2(8)$	0.750			0.435	0.159	
<u>Table Entries:</u>	250.0			750.0	750.0	
<u>Upper Entry</u> absorption coefficient (km^{-1})	1.130					
	500.0					
<u>Lower Entry</u> air buffer pressure (torr)	1.506					
	750.0					

$P_3(5)$	0.680					
<u>Table Entries:</u>	60.70					
<u>Upper Entry</u> absorption coefficient (km^{-1})	3.358					
	750.0					
<u>Lower Entry</u> air buffer pressure (torr)						

REFERENCES

1. McClatchey, R. A., W. S. Benedict, S. A. Clough, D. E. Burch, R. E. Calfee, K. Fox, L. S. Rothman, and J. S. Garing, "AFGL Atmospheric Absorption Line Parameter Compilation," AFGRL-TR-73-0096, 1973.
2. Watkins, W. R., and R. G. Dixon, "Automation of Long-Path Absorption Cell Measurements," ECOM-5821, Atmospheric Sciences Laboratory, US Army Electronics Command, White Sands Missile Range, NM, June 1977.
3. Watkins, W. R., "Path Differencing: An Improvement to Multipass Absorption Cell Measurements," Applied Optics 15, 16 (1976).
4. White, K. O., G. T. Wade, and S. A. Schleusener, "The Application of Minicomputers in Laser Atmospheric Experiments," Proceedings of the IEEE 61, 1956 (1973).
5. Van Vleck, J. H., and V. F. Weisskopf, "On the Shape of Collision-Broadened Lines," Reviews of Modern Physics 17, 227 (1945).
6. Penner, S. S., Quantitative Molecular Spectroscopy and Gas Emissivities, Addison-Wesley Publishing Co., Reading, MA (1959).
7. Pierluissi, J. H., P. C. Vanderwood, and R. B. Gomez, "Fast Computational Algorithm for the Voigt Profiles," J. Quant. Spec. Rad. Trans. 18, 555 (1977).
8. Flaud, J. M., and C. Camy-Peyret, "Vibration-Rotation Intensities in H₂O-Type Molecules Application to the 2V₂, V₁, and V₃ Bands of H₂¹⁶O," J. Molec. Spec. 55, 278 (1975).
9. Herzberg, G., Molecular Spectra and Molecular Structure II Infrared and Raman Spectra of Polyatomic Molecules, D. Van Nostrand Co., Inc., Princeton, NJ, 1960.
10. Benedict, W. S., and L. D. Kaplan, "Calculation of Line Widths in H₂O - N₂ Collisions," J. Chem. Phys. 30, 388 (1959).
11. Burch, D. E., E. B. Singleton, and D. Williams, "Absorption Line Broadening in the Infrared," Applied Optics 1, 359 (1962).
12. Burch, D. E., D. A. Gryvnak, R. R. Patty, and C. E. Bartky, "Absorption of Infrared Radiant Energy by CO₂ and H₂O. IV Shapes of Collision Broadened CO₂ Lines," J. Opt. Soc. Am. 59, 267 (1969).
13. Tanaka, M., and T. Yamanouchi, "Absorption Properties of the Near Infrared CO₂ Bands," J. Quant. Spec. Rad. Trans. 17, 421 (1977).

14. Burch, D. E., "Semi-Annual Technical Report Investigation of the Absorption of Infrared Radiation by Atmospheric Gases," Ford Aero-neutronic Report No. U-4784, January 1970.
15. Long, R. K., F. S. Mills, and G. L. Trusty, "Experimental Absorption Coefficients for Eleven CO Laser Lines," The Ohio State University Electroscience Laboratory Report No. 3271-5, March 1973.
16. Benedict, W. S., "The Strength, Width, and Shapes of Infrared Lines. I General Considerations," Canadian J. of Phys. 34, 847 (1951).
17. Pugh, L. A., and K. N. Rao, "Spectrum of Water Vapor in the 1.9 and 2.7 μ Regions," J. Mol. Spec. 47, 403 (1973).
18. Randall, C. M., "Monochromatic Transmittance/Radiance Computations," SAMSO Report No. TR-74-247, Chemistry and Physics Laboratory - The Aerospace Corporation, December 1974.
19. Gray, L. D., and J. E. Selvidge, "Relative Intensity Calculations for Carbon Dioxide," J. Quant. Spec. Rad. Trans. 5, 291 (1965).
20. LaRocca, A. J., and R. G. Turner, "Atmospheric Transmittance and Radiance: Methods of Calculation," Environmental Research Institute of Michigan, Report No. 107600-10-I, June 1975, 431.

DISTRIBUTION LIST

Commander
US Army Aviation Center
ATTN: ATZQ-D-MA
Fort Rucker, AL 36362

Chief, Atmospheric Sciences Div
Code ES-81
NASA
Marshall Space Flight Center,
AL 35812

Commander
US Army Missile Command
ATTN: DRSMI-RRA, Bldg 7770
Redstone Arsenal, AL 35809

Commander
US Army Missile Command
ATTN: DRDMI-TEM
Redstone Arsenal, AL 35809

Commander
US Army Missile Rsch & Dev Command
ATTN: DRDMI-TR
Redstone Arsenal, AL 35809

Commander
US Army Missile Rsch & Dev Command
ATTN: DRDMI-CGA (B. W. Fowler)
Redstone Arsenal, AL 35809

Redstone Scientific Information Ctr
ATTN: DRDMI-TBD
US Army Missile Rsch & Dev Command
Redstone Arsenal, AL 35809

Commander
HQ, Fort Huachuca
ATTN: Tech Ref Div
Fort Huachuca, AZ 85613

Commander
US Army Intelligence Ctr & School
ATTN: ATSI-CD-MD
Fort Huachuca, AZ 85613

Commander
US Army Proving Ground
ATTN: Technical Library
Bldg 2100
Yuma, AZ 85364

Naval Weapons Ctr (Code 3173)
ATTN: Dr. A. Shlanta
China Lake, CA 93555

Sylvania Elec Sys Western Div
ATTN: Technical Reports Library
PO Box 205
Mountain View, CA 94040

Range Commanders Council
ATTN: Mr. Hixon
PMTC Code 3252
Pacific Missile Test Center
Point Mugu, CA 93042

Commander
Naval Ocean Systems Center
ATTN: Research Library
San Diego, CA 92152

Meteorologist in Charge
Kwajalein Missile Range
PO Box 67
APO
San Francisco, CA 96555

Director
Atmospheric Physics & Chem Lab
Code R31, NOAA
Department of Commerce
Boulder, CO 80302

Library-R-51-Tech Reports
Environmental Research Labs
NOAA
Boulder, CO 80302

National Center for Atmos Res
NCAR Library
PO Box 3000
Boulder, CO 80307

R. B. Girardo
Bureau of Reclamation
E&R Center, Code 1220
Denver Federal Ctr, Bldg 67
Denver, CO 80225

Head, Atmospheric Rsch Section
National Science Foundation
1800 G. Street, NW
Washington, DC 20550

Defense Communications Agency
Technical Library Center
Code 205
Washington, DC 20305

Director
Defense Nuclear Agency
ATTN: Tech Library
Washington, DC 20305

HQDA (DAEN-RDM/Dr. De Percin)
Forrestal Bldg
Washington, DC 20314

CPT Hugh Albers, Exec Sec
Interdept Committee on Atmos Sci
Fed Council for Sci & Tech
National Sci Foundation
Washington, DC 20550

The Library of Congress
ATTN: Exchange & Gift Div
Washington, DC 20540
2

Mil Assistant for
Environmental Sciences
DAD (E & LS), 3D129
The Pentagon
Washington, DC 20301

National Weather Service
National Meteorological Center
World Weather Bldg-5200 Auth Rd
ATTN: Mr. Quiroz
Washington, DC 20233

Dir, US Naval Research Lab
Code 5530
Washington, DC 20375

Commanding Officer
Naval Research Laboratory
Code 2627
Washington, DC 20375

Office, Asst Sec Army (R&D)
ATTN: Dep for Science & Tech
HQ, Department of the Army
Washington, DC 20310

Director, Systems R&D Service
Federal Aviation Administration
ATTN: ARD-54
2100 Second Street, SW
Washington, DC 20590

Dr. John L. Walsh
Code 4109
Navy Research Lab
Washington, DC 20375

Armament Dev & Test Center
ADTC (DLOSL)
Eglin AFB, FL 32542

Naval Training Equipment Center
ATTN: Technical Library
Orlando, FL 32813

Det 1, SAMTEC
TOEL - ATTN: Maj Orondorff
Patrick AFB, FL 32925

HQ, ESD/DRI/S-22
Hanscom AFB
Bedford, MA 01731

Air Force Cambridge Rsch Labs
ATTN: LCB (A. S. Carten, Jr.)
Hanscom AFB
Bedford, MA 01731

Air Force Geophysics Laboratory
ATTN: LYD
Hanscom AFB
Bedford, MA 01731

Meteorology Laboratory
AFGL/LY
Hanscom AFB
Bedford, MA 01731

US Army Liaison Office
MIT-Lincoln Lab, Library A-082
PO Box 73
Lexington, MA 02173

AD-A059 969

ARMY ELECTRONICS RESEARCH AND DEVELOPMENT COMMAND WS--ETC F/G 4/1
WATER VAPOR ABSORPTION COEFFICIENTS AT HF LASER WAVELENGTHS. PA--ETC(U).
MAY 78 W R WATKINS, R L SPELLICY, K O WHITE
ERADCOM/ASL-TR-0007-PT-1

UNCLASSIFIED

NL

2 OF 2
ADA
069969



END
DATE
FILMED
12-78
DDC

Director
US Army Armament Rsch & Dev Com
Chemical Systems Laboratory
ATTN: DRDAR-CLJ-I
APG, MD 21010

Commander
US Army Ballistic Rsch Labs
ATTN: DRXBR-IB
APG, MD 21005

Director
US Army Ballistic Rsch Labs
ATTN: DRDAR-BLB (Dr. G. E. Keller)
APG, MD 21005

Commanding General
ERADCOM
ATTN: DRDEL-AP
2800 Powder Mill Road
Adelphi, MD 20783
2

Commanding General
ERADCOM
ATTN: DRDEL-CG/DRDEL-DC/DRDEL-CS
2800 Powder Mill Road
Adelphi, MD 20783

Commanding General
ERADCOM
ATTN: DRDEL-CT
2800 Powder Mill Road
Adelphi, MD 20783
2

Commanding General
ERADCOM
ATTN: DRDEL-LL/DRDEL-SB/DRDEL-EA
2800 Powder Mill Road
Adelphi, MD 20783

Commanding General
ERADCOM
ATTN: DRDEL-PA/DRDEL-ILS/DRDEL-E
2800 Powder Mill Road
Adelphi, MD 20783

Commanding General
ERADCOM
ATTN: DRDEL-PAO (S. Kimmel)
2800 Powder Mill Road
Adelphi, MD 20783

Commanding General
ERADCOM
ATTN: DRDEL-PR
2800 Powder Mill Road
Adelphi, MD 20783

Commander
Harry Diamond Laboratories
ATTN: DELHD-CO
2800 Powder Mill Road
Adelphi, MD 20783

Dir of Dev & Engr
Defense Systems Div
ATTN: SAREA-DE-DDR
(H. Tannenbaum)
Edgewood Arsenal, APG, MD 21010

Dir National Security Agency
ATTN: TDL (C513)
Fort George G. Meade, MD 20755

Commander
Intelligence Materiel Dev & Support Ofc
ATTN: DELEW-WL-I
Bldg 4554
Fort George G. Meade, MD 20755

Technical Processes Br-D823
NOAA, Lib & Info Serv Div
6009 Executive Blvd
Rockville, MD 20852

Naval Surface Weapons Center
Technical Library & Information
Services Division
White Oak, Silver Spring, MD
20910

The Environmental Rsch
Institute of MI
ATTN: IRIA Library
PO Box 618
Ann Arbor, MI 48107

Mr. William A. Main
USDA Forest Service
1407 S. Harrison Road
East Lansing, MI 48823

Dr. A. D. Belmont
Research Division
PO Box 1249
Control Data Corp
Minneapolis, MN 55440

Dir, Naval Oceanography & Meteorology
National Space Technology Labs
Bay St Louis, MS 39529

Director
USAE Waterways Experiment Station
ATTN: Library
PO Box 631
Vicksburg, MS 39180

Director
US Army Engr Waterways Exper Sta
ATTN: Library Branch
Vicksburg, MS 39180

Environmental Protection Agency
Meteorology Laboratory
Research Triangle Park, NC 27711

US Army Research Office
ATTN: DRXRO-IP
PO Box 12211
Research Triangle Park, NC 27709

Commander
Combat Surveillance & Target
Acquisition Laboratory
Fort Monmouth, NJ 07703

Commander
Electronic Technology & Devices Lab
ATTN: DELET-D
Fort Monmouth, NJ 07703

Commander
Electronic Warfare Laboratory
ATTN: DELEW-D
Fort Monmouth, NJ 07703

Commander
Night Vision & Electro-Optics Labs
ATTN: DELNV-L (Dr. Rudolf Buser)
Fort Monmouth, NJ 07703

Commander
ERADCOM
Technical Support Activity
ATTN: DELSD-D
Fort Monmouth, NJ 07703

Commander
ERADCOM Tech Support Directorate
Technical Library Division
ATTN: DELSD-L
Fort Monmouth, NJ 07703

Commander
Department of the Army
Project Manager, FIREFINDER
ATTN: DRCPM-FF
Fort Monmouth, NJ 07703

Commander
Department of the Army
Project Manager, REMBASS
ATTN: DRCPM-RBS
Fort Monmouth, NJ 07703

Commander
US Army Satellite Comm Agc
ATTN: DRCPM-SC-3
Fort Monmouth, NJ 07703

Commander
Department of the Army
Project Manager, SOTAS
ATTN: DRCPM-STA
Fort Monmouth, NJ 07703

Commander
ERADCOM Scientific Advisor
ATTN: DRDEL-SA
Fort Monmouth, NJ 07703

Commander
US Army Electronics Command
ATTN: DRSEL-CT-S
Fort Monmouth, NJ 07703

Commander
US Army Electronics Command
ATTN: DRSEL-CT-S (Dr. Swingle)
Fort Monmouth, NJ 07703

Commander
ATTN: DRSEL-VL-D
Fort Monmouth, NJ 07703

Commander
US Army Electronics Command
ATTN: DRSEL-WL-D1
Fort Monmouth, NJ 07703

Commanding Officer
US Army Armament Rsch & Dev Com
ATTN: DRDAR-TSS #59
Dover, NJ 07801

Commander
Aviation Flight Test Activity
ATTN: DELAF-CO
Lakehurst NAEC, NJ 08733

6585 TG/WE
Holloman AFB, NM 88330

Commander
AFWL/WE
Kirtland AFB, NM 87117

Air Force Weapons Laboratory
ATTN: Technical Library (SUL)
Kirtland AFB, NM 87117

Commander
US Army Test & Evaluation Command
ATTN: Technical Library
White Sands Missile Range, NM 88002

Rome Air Development Center
ATTN: Documents Library
TILD (Bette Smith)
Griffiss AFB, NY 13441

Commander
US Army Tropic Test Center
ATTN: STETC-MO (Tech Library)
APO New York 09827

Commandant
USAFAS
ATTN: ATSF-CD-MT (Mr. Farmer)
Fort Sill, OK 73503

Commandant
US Army Field Artillery School
ATTN: ATSF-CF-R
Fort Sill, OK 73503

Director CFD
US Army Field Artillery School
ATTN: Met Division
Fort Sill, OK 73503

Commandant
US Army Field Artillery School
ATTN: Morris Swett Tech Library
Fort Sill, OK 73503

Commander
US Army Dugway Proving Ground
ATTN: MT-S
Dugway, UT 84022

William Peterson
Research Association
Utah State University, UNC 48
Logan, UT 84322

Inge Dirmhirn, Professor
Utah State University, UMC 48
Logan, UT 84322

Defense Documentation Center
ATTN: DDC-TCA
Cameron Station (Bldg 5)
Alexandria, VA 22314
12

Commander
Department of the Army
PM, Concept Analysis Center
ATTN: ORCPM-CAC, Arlington Hall Sta
Arlington, VA 22312

Commander
Signals Warfare Laboratory
ATTN: DELSW-D
Arlington Hall Station
Arlington, VA 22312

Commander
US Army INSCOM
ATTN: IARDA-OS
Arlington Hall Station
Arlington, VA 22212

CO, USA Foreign Sci & Tech Center
ATTN: DRXST-ISI
220 7th Street, NE
Charlottesville, VA 22901

USAFETAC/CB (Stop 825)
Scott AFB, IL 62225

Naval Surface Weapons Center
Code DT-22 (Ms. Greeley)
Dahlgren, VA 22448

Commander
Night Vision & Electro-Optics Labs
ATTN: DELNV-D
Fort Belvoir, VA 22060

Commander and Director
US Army Engineer Topographic Labs
ETL-GS-AC
Fort Belvoir, VA 22060

US Army Nuclear Agency
ATTN: MONA-WE
Fort Belvoir, VA 22060

Commander
Eustis Directorate
US Army Air Mobility R&D Lab
ATTN: Technical Library
Fort Eustis, VA 23604

Department of the Air Force
OL-C, 5WW
Fort Monroe, VA 23651

Department of the Air Force
5 WW/DN
Langley AFB, VA 23665

Director
Development Center MCDEC
ATTN: Firepower Division
Quantico, VA 22134

Commander
USA Cold Regions Test Center
ATTN: STECR-OP-PM
APO Seattle 98733

Dr. Frank D. Eaton
PO Box 3038
University Station
Laramie, WY 82071

ATMOSPHERIC SCIENCES RESEARCH PAPERS

1. Lindberg, J.D., "An Improvement to a Method for Measuring the Absorption Coefficient of Atmospheric Dust and other Strongly Absorbing Powders," ECOM-5565, July 1975.
2. Avara, Elton, P., "Mesoscale Wind Shears Derived from Thermal Winds," ECOM-5566, July 1975.
3. Gomez, Richard B., and Joseph H. Pierluissi, "Incomplete Gamma Function Approximation for King's Strong-Line Transmittance Model," ECOM-5567, July 1975.
4. Blanco, A.J., and B.F. Engebos, "Ballistic Wind Weighting Functions for Tank Projectiles," ECOM-5568, August 1975.
5. Taylor, Fredrick J., Jack Smith, and Thomas H. Pries, "Crosswind Measurements through Pattern Recognition Techniques," ECOM-5569, July 1975.
6. Walters, D.L., "Crosswind Weighting Functions for Direct-Fire Projectiles," ECOM-5570, August 1975.
7. Duncan, Louis D., "An Improved Algorithm for the Iterated Minimal Information Solution for Remote Sounding of Temperature," ECOM-5571, August 1975.
8. Robbiani, Raymond L., "Tactical Field Demonstration of Mobile Weather Radar Set AN/TPS-41 at Fort Rucker, Alabama," ECOM-5572, August 1975.
9. Miers, B., G. Blackman, D. Langer, and N. Lorimier, "Analysis of SMS/GOES Film Data," ECOM-5573, September 1975.
10. Manquero, Carlos, Louis Duncan, and Rufus Bruce, "An Indication from Satellite Measurements of Atmospheric CO₂ Variability," ECOM-5574, September 1975.
11. Petracca, Carmine, and James D. Lindberg, "Installation and Operation of an Atmospheric Particulate Collector," ECOM-5575, September 1975.
12. Avara, Elton P., and George Alexander, "Empirical Investigation of Three Iterative Methods for Inverting the Radiative Transfer Equation," ECOM-5576, October 1975.
13. Alexander, George D., "A Digital Data Acquisition Interface for the SMS Direct Readout Ground Station - Concept and Preliminary Design," ECOM-5577, October 1975.
14. Cantor, Israel, "Enhancement of Point Source Thermal Radiation Under Clouds in a Nonattenuating Medium," ECOM-5578, October 1975.
15. Norton, Colburn, and Glenn Hoidale, "The Diurnal Variation of Mixing Height by Month over White Sands Missile Range, N.M.," ECOM-5579, November 1975.
16. Avara, Elton P., "On the Spectrum Analysis of Binary Data," ECOM-5580, November 1975.
17. Taylor, Fredrick J., Thomas H. Pries, and Chao-Huan Huang, "Optimal Wind Velocity Estimation," ECOM-5581, December 1975.
18. Avara, Elton P., "Some Effects of Autocorrelated and Cross-Correlated Noise on the Analysis of Variance," ECOM-5582, December 1975.
19. Gillespie, Patti S., R.L. Armstrong, and Kenneth O. White, "The Spectral Characteristics and Atmospheric CO₂ Absorption of the Ho⁺³-YLF Laser at 2.05 μ m," ECOM-5583, December 1975.
20. Novlan, David J., "An Empirical Method of Forecasting Thunderstorms for the White Sands Missile Range," ECOM-5584, February 1976.
21. Avara, Elton P., "Randomization Effects in Hypothesis Testing with Autocorrelated Noise," ECOM-5585, February 1976.
22. Watkins, Wendell R., "Improvements in Long Path Absorption Cell Measurement," ECOM-5586, March 1976.
23. Thomas, Joe, George D. Alexander, and Marvin Dubbin, "SATTEL - An Army Dedicated Meteorological Telemetry System," ECOM-5587, March 1976.
24. Kennedy, Bruce W., and Delbert Bynum, "Army User Test Program for the RDT&E-XM-75 Meteorological Rocket," ECOM-5588, April 1976.

25. Barnett, Kenneth M., "A Description of the Artillery Meteorological Comparisons at White Sands Missile Range, October 1974 - December 1974 ('PASS' - Prototype Artillery [Meteorological] Subsystem)," ECOM-5589, April 1976.
26. Miller, Walter B., "Preliminary Analysis of Fall-of-Shot From Project 'PASS'," ECOM-5590, April 1976.
27. Avara, Elton P., "Error Analysis of Minimum Information and Smith's Direct Methods for Inverting the Radiative Transfer Equation," ECOM-5591, April 1976.
28. Yee, Young P., James D. Horn, and George Alexander, "Synoptic Thermal Wind Calculations from Radiosonde Observations Over the Southwestern United States," ECOM-5592, May 1976.
29. Duncan, Louis D., and Mary Ann Seagraves, "Applications of Empirical Corrections to NOAA-4 VTPR Observations," ECOM-5593, May 1976.
30. Miers, Bruce T., and Steve Weaver, "Applications of Meteorological Satellite Data to Weather Sensitive Army Operations," ECOM-5594, May 1976.
31. Sharenow, Moses, "Redesign and Improvement of Balloon ML-566," ECOM-5595, June, 1976.
32. Hansen, Frank V., "The Depth of the Surface Boundary Layer," ECOM-5596, June 1976.
33. Pinnick, R.G., and E.B. Stenmark, "Response Calculations for a Commercial Light-Scattering Aerosol Counter," ECOM-5597, July 1976.
34. Mason, J., and G.B. Hoidale, "Visibility as an Estimator of Infrared Transmittance," ECOM-5598, July 1976.
35. Bruce, Rufus E., Louis D. Duncan, and Joseph H. Pierluissi, "Experimental Study of the Relationship Between Radiosonde Temperatures and Radiometric-Area Temperatures," ECOM-5599, August 1976.
36. Duncan, Louis D., "Stratospheric Wind Shear Computed from Satellite Thermal Sounder Measurements," ECOM-5800, September 1976.
37. Taylor, F., P. Mohan, P. Joseph and T. Pries, "An All Digital Automated Wind Measurement System," ECOM-5801, September 1976.
38. Bruce, Charles, "Development of Spectrophones for CW and Pulsed Radiation Sources," ECOM-5802, September 1976.
39. Duncan, Louis D., and Mary Ann Seagraves, "Another Method for Estimating Clear Column Radiances," ECOM-5803, October 1976.
40. Blanco, Abel J., and Larry E. Taylor, "Artillery Meteorological Analysis of Project Pass," ECOM-5804, October 1976.
41. Miller, Walter, and Bernard Engebos, "A Mathematical Structure for Refinement of Sound Ranging Estimates," ECOM-5805, November, 1976.
42. Gillespie, James B., and James D. Lindberg, "A Method to Obtain Diffuse Reflectance Measurements from 1.0 to 3.0 μ m Using a Cary 17I Spectrophotometer," ECOM-5806, November 1976.
43. Rubio, Roberto, and Robert O. Olsen, "A Study of the Effects of Temperature Variations on Radio Wave Absorption," ECOM-5807, November 1976.
44. Ballard, Harold N., "Temperature Measurements in the Stratosphere from Balloon-Borne Instrument Platforms, 1968-1975," ECOM-5808, December 1976.
45. Monahan, H.H., "An Approach to the Short-Range Prediction of Early Morning Radiation Fog," ECOM-5809, January 1977.
46. Engebos, Bernard Francis, "Introduction to Multiple State Multiple Action Decision Theory and Its Relation to Mixing Structures," ECOM-5810, January 1977.
47. Low, Richard D.H., "Effects of Cloud Particles on Remote Sensing from Space in the 10-Micrometer Infrared Region," ECOM-5811, January 1977.
48. Bonner, Robert S., and R. Newton, "Application of the AN/GVS-5 Laser Rangefinder to Cloud Base Height Measurements," ECOM-5812, February 1977.
49. Rubio, Roberto, "Lidar Detection of Subvisible Reentry Vehicle Erosive Atmospheric Material," ECOM-5813, March 1977.
50. Low, Richard D.H., and J.D. Horn, "Mesoscale Determination of Cloud-Top Height: Problems and Solutions," ECOM-5814, March 1977.

51. Duncan, Louis D., and Mary Ann Seagraves, "Evaluation of the NOAA-4 VTPR Thermal Winds for Nuclear Fallout Predictions," ECOM-5815, March 1977.
52. Randhawa, Jagir S., M. Izquierdo, Carlos McDonald and Zvi Salpeter, "Stratospheric Ozone Density as Measured by a Chemiluminescent Sensor During the Stratcom VI-A Flight," ECOM-5816, April 1977.
53. Rubio, Roberto, and Mike Izquierdo, "Measurements of Net Atmospheric Irradiance in the 0.7- to 2.8-Micrometer Infrared Region," ECOM-5817, May 1977.
54. Ballard, Harold N., Jose M. Serna, and Frank P. Hudson Consultant for Chemical Kinetics, "Calculation of Selected Atmospheric Composition Parameters for the Mid-Latitude, September Stratosphere," ECOM-5818, May 1977.
55. Mitchell, J.D., R.S. Sagar, and R.O. Olsen, "Positive Ions in the Middle Atmosphere During Sunrise Conditions," ECOM-5819, May 1977.
56. White, Kenneth O., Wendell R. Watkins, Stuart A. Schleusener, and Ronald L. Johnson, "Solid-State Laser Wavelength Identification Using a Reference Absorber," ECOM-5820, June 1977.
57. Watkins, Wendell R., and Richard G. Dixon, "Automation of Long-Path Absorption Cell Measurements," ECOM-5821, June 1977.
58. Taylor, S.E., J.M. Davis, and J.B. Mason, "Analysis of Observed Soil Skin Moisture Effects on Reflectance," ECOM-5822, June 1977.
59. Duncan, Louis D. and Mary Ann Seagraves, "Fallout Predictions Computed from Satellite Derived Winds," ECOM-5823, June 1977.
60. Snider, D.E., D.G. Murcray, F.H. Murcray, and W.J. Williams, "Investigation of High-Altitude Enhanced Infrared Background Emissions" (U), SECRET, ECOM-5824, June 1977.
61. Dubbin, Marvin H. and Dennis Hall, "Synchronous Meteorological Satellite Direct Readout Ground System Digital Video Electronics," ECOM-5825, June 1977.
62. Miller, W., and B. Engebos, "A Preliminary Analysis of Two Sound Ranging Algorithms," ECOM-5826, July 1977.
63. Kennedy, Bruce W., and James K. Luers, "Ballistic Sphere Techniques for Measuring Atmospheric Parameters," ECOM-5827, July 1977.
64. Duncan, Louis D., "Zenith Angle Variation of Satellite Thermal Sounder Measurements," ECOM-5828, August 1977.
65. Hansen, Frank V., "The Critical Richardson Number," ECOM-5829, September 1977.
66. Ballard, Harold N., and Frank P. Hudson (Compilers), "Stratospheric Composition Balloon-Borne Experiment," ECOM-5830, October 1977.
67. Barr, William C., and Arnold C. Peterson, "Wind Measuring Accuracy Test of Meteorological Systems," ECOM-5831, November 1977.
68. Ethridge, G.A. and F.V. Hansen, "Atmospheric Diffusion: Similarity Theory and Empirical Derivations for Use in Boundary Layer Diffusion Problems," ECOM-5832, November 1977.
69. Low, Richard D.H., "The Internal Cloud Radiation Field and a Technique for Determining Cloud Blackness," ECOM-5833, December 1977.
70. Watkins, Wendell R., Kenneth O. White, Charles W. Bruce, Donald L. Walters, and James D. Lindberg, "Measurements Required for Prediction of High Energy Laser Transmission," ECOM-5834, December 1977.
71. Rubio, Robert, "Investigation of Abrupt Decreases in Atmospherically Backscattered Laser Energy," ECOM-5835, December 1977.
72. Monahan, H.H. and R.M. Cionco, "An Interpretative Review of Existing Capabilities for Measuring and Forecasting Selected Weather Variables (Emphasizing Remote Means)," ASL-TR-0001, January 1978.
73. Heaps, Melvin G., "The 1979 Solar Eclipse and Validation of D-Region Models," ASL-TR-0002, March 1978.

74. Jennings, S.G., and J.B. Gillespie, "M.I.E. Theory Sensitivity Studies - The Effects of Aerosol Complex Refractive Index and Size Distribution Variations on Extinction and Absorption Coefficients Part II: Analysis of the Computational Results," ASL-TR-0003, March 1978.
75. White, Kenneth O. et al, "Water Vapor Continuum Absorption in the 3.5 μ m to 4.0 μ m Region," ASL-TR-0004, March 1978.
76. Olsen, Robert O., and Bruce W. Kennedy, "ABRES Pretest Atmospheric Measurements," ASL-TR-0005, April 1978.
77. Ballard, Harold N., Jose M. Serna, and Frank P. Hudson, "Calculation of Atmospheric Composition in the High Latitude September Stratosphere," ASL-TR-0006, May 1978.
78. Watkins, Wendell R. et al, "Water Vapor Absorption Coefficients at HF Laser Wavelengths," ASL-TR-0007, May 1978.